A theoretical model for solving wave scattering by multiple submerged horizontal plates and membranes

S. Zheng[a,b], G. Sun[a], H. Liang[c,*], A. G. L. Borthwick, D. M. Greaves

[a] *State Key Laboratory of Ocean Sensing & Ocean College, Zhejiang University, Zhoushan, 316021, P.R. China*
[b] *School of Engineering, Computing & Mathematics, University of Plymouth, Drake Circus, Plymouth PL4 8AA, UK*
[c] *Technology Centre for Offshore and Marine, Singapore (TCOMS), 118411, Singapore*

Abstract

This paper presents a theoretical model for water wave scattering by arrays of submerged horizontal plates and membranes. Based on linear potential flow theory and the Fourier transform, the model overcomes limitations of eigenfunction matching by accommodating arbitrary plate arrangements. The potential jump across the plate is represented using Chebyshev polynomial expansions that inherently capture edge singularities, ensuring rapid convergence. A key theoretical finding proves that swapping the positions of two staggered porous flexible plates leaves the wave transmission coefficient unchanged across all frequencies. For coaxial dual plates, the reflection coefficient exhibits bimodal peaks. Staggered or side-by-side configurations shift these peaks lower and enhance short-wave attenuation. Larger plate spacing amplifies force oscillations on the seaward plate due to wave interference. The model is extended to analyse wave scattering by metastructures with square, circular, trapezoidal, and inverted trapezoidal profiles. The inverted trapezoidal design enhances low-frequency reflection through its extended shallow plates, while its deeper elements reduce short-wave interaction, enabling optimised performance for coastal protection applications.

Keywords: Wave-structure interactions, Submerged plates/membranes, Hydroelasticity

1. Introduction

Submerged structures are increasingly preferred for coastal protection worldwide due to their cost-effectiveness and low visual impact. They provide a practical solution where complete wave blocking is not necessary and some wave energy transmission is beneficial, such as in stabilising replenished beaches [1] or reducing sedimentation in channels and harbours [2, 3]. Compared to floating alternatives, submerged plates and membranes are less vulnerable to severe wave breaking and have reduced physical and environmental impacts. Their low construction cost is a significant advantage. The foregoing benefits make submerged plates and membranes particularly suitable for protecting natural beaches and harnessing marine renewable energy.

The foundation for understanding wave interactions with single submerged structures is well-established. Extensive research, utilising methods like eigenfunction matching, integral equations, and the Wiener-Hopf technique, has thoroughly investigated the hydrodynamics of rigid impermeable plates [4, 5, 6], porous

*Corresponding author
Email address: liang_hui@tcoms.sg (H. Liang)

plates [7, 8, 9, 10, 11], and flexible membranes/elastic plates [12, 13, 14]. These studies have shown that porosity enhances energy dissipation, while flexibility allows resonance tuning, improving wave attenuation performance. The interaction of waves with structures that are both porous and flexible introduces further complexity, but has also been addressed for single elements [15, 16], including novel applications in wave energy conversion [17, 18, 19] where energy harvesting is achieved by using piezoelectric materials.

For many practical applications however, a single plate is insufficient to achieve the desired performance metrics, such as in broadband wave attenuation or targeted wave focusing. This has spurred interest in multi-element configurations, such as dual-layer plates, arrays, and engineered metastructures [20, 21]. Research on these systems has, to date, been constrained by significant methodological limitations. Existing semi-analytical approaches, primarily based on eigenfunction matching, are only tractable for coaxial and side-by-side arrangements. Coaxial configuration models exist for multiple identical plates stacked coaxially [22], upper porous/lower solid combinations [23], two coaxial submerged horizontal porous plates [24], and multi-layer porous plate configurations [25]. Side-by-side array solutions have been developed for arrays of identical plates with uniform properties and submergence [26]. The critical research challenge in the field is the current inability to efficiently model wave scattering by arrays of plates with non-identical properties, and arbitrary spatial arrangement (e.g., staggered plates). A fundamental complication arises from the need to accurately resolve fluid velocity singularities at the edges of each plate, a feature that is difficult to handle in multi-domain potential flow models and is often neglected or approximated, affecting the convergence properties [27]. Our recent work [20] addressed this challenge and employed the Hankel transform approach to study wave scattering by submerged disk arrays. However, to the best of our knowledge, a robust, flexible theoretical framework capable of modelling wave interaction with arrays of submerged rectangular flexible and/or porous plates has yet to be reported. This gap prevents the systematic exploration and optimisation of metastructures for advanced coastal protection and energy harvesting.

Our current work directly addresses this challenge. We present a theoretical model for linear water wave scattering by arrays of submerged horizontal rectangular plates and membranes with arbitrary spacing, and arrangement. Unlike our previous Hankel transform-based model that was developed for an array of submerged disks [20], the present model overcomes the limitations of eigenfunction matching by leveraging the Fourier transform. Velocity potential discontinuities across the plates are expanded using Chebyshev polynomials of the second kind, which inherently capture the correct edge singularity behaviour, ensuring rapid convergence without a priori assumptions about the flow. Techniques based on the Fourier transform and expansion in Chebyshev polynomials of the second kind were also applied by Porter [6] to wave scattering by a submerged horizontal rigid plate, and by Liang *et al.* [21] to wave scattering by an array of vertical rigid plates. This approach allows us to efficiently investigate previously intractable configurations, including: coaxial, staggered, and side-by-side, with non-identical plates. The model is rigorously verified against established benchmark solutions. It is then employed to provide new insight into the hydrodynamic performance of multi-plate systems, analysing the effects of configuration, spacing, and metastructure shape on reflection, transmission, and force distribution. A key finding is that for two staggered porous flexible plates, swapping their positions alters the reflection coefficient and power dissipation, yet the transmis-

sion coefficient remains constant across all wave frequencies, a non-intuitive result with significant design implications.

The remainder of the paper is structured as follows. In §2, we pose the problem statement and then derive expressions for wave power dissipation due to porosity of the plates and membranes, the free-surface elevation, and wave forces and moments acting on the structures. §3 describes the model verification tests. §4 presents sets of results from parameter tests for wave interaction with dual porous flexible plates and the wave scattering of metastructures consisting of horizontal rigid plate arrays. The main findings are summarised in §5.

2. Mathematical model

We consider wave scattering by N ($N \geq 1$) submerged horizontal rectangular plates or membranes placed as shown in Fig. 1. A global Cartesian coordinate system $Oxyz$ is chosen with the mean free–surface coinciding with the (x, y)–plane and Oz pointing vertically upwards. The bottom of the fluid domain is located at $z = -h$, where h is the still water depth. Incident waves propagate forward along the Ox axis. The dimension of the structures in the Oy direction is assumed to be much larger than the incident wavelength, so that the wave scattering problem can be treated as a 2D problem in the (x, z)–plane.

The plates/membranes are assumed sufficiently thin that their thickness does not influence the flow field. The n-th ($n = 1, 2, \cdots, N$) plate/membrane is $2a_n$ long in the Ox direction and submerged underwater at a depth of d_n below still water level. The centre of the plate/membrane is x_n away from the origin of the coordinate system, i.e., the (y, z)–plane.

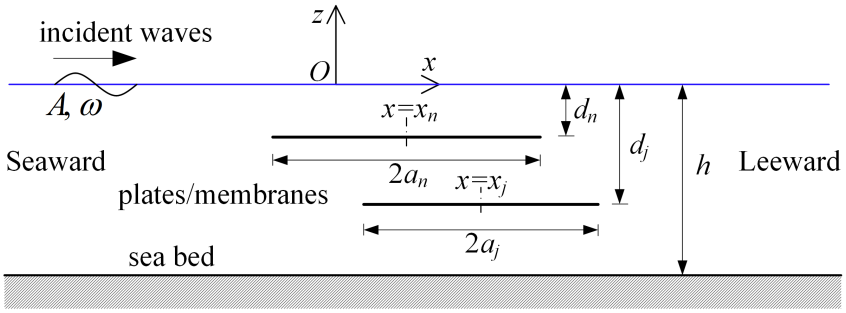

Figure 1: Side view of multiple submerged horizontal plates/membranes.

We assume that all amplitudes are sufficiently small that linear theory applies, and we make the usual assumptions that the fluid is inviscid, incompressible, and its motion is irrotational. We denote the fluid velocity potential by $\Phi(x, z, t)$. It is further assumed that all motion is time-harmonic with an angular frequency ω. Thus, we can write

$$\Phi(x, z, t) = \mathrm{Re}\{\phi(x, z)\mathrm{e}^{-\mathrm{i}\omega t}\}, \tag{1}$$

where Re denotes the real part, ϕ is the spatial velocity potential which is independent of time t, and i is the imaginary unit.

2.1. Governing equation and boundary conditions

The velocity potential may be divided into two components as

$$\phi = \phi_I + \phi_D, \tag{2}$$

where ϕ_I denotes the undisturbed incident wave potential

$$\phi_I(x,z) = \frac{-\mathrm{i}gA}{\omega\cosh(kh)}\mathrm{e}^{\mathrm{i}kx}\psi(z) \tag{3}$$

in which k is the wavenumber, A is the wave amplitude, g is the acceleration due to gravity, $\psi(z) = \cosh[k(z+h)]$, and ϕ_D represents the diffracted wave velocity potential.

The diffracted velocity potential ϕ_D could be further expanded as

$$\phi_D(x,z) = \sum_{n=1}^{N}\phi_n(x,z), \tag{4}$$

where $\phi_n(x,z)$ is associated with the pressure jump across the n-th plate/membrane, and is discontinuous at $|x-x_n| < a_n$, $z = -d_n$ and continuous elsewhere.

ϕ_n satisfies the Laplace equation,

$$\left(\frac{\partial^2}{\partial x^2} + \frac{\partial^2}{\partial z^2}\right)\phi_n = 0 \quad \text{in the water}, \tag{5}$$

the free surface boundary condition,

$$\frac{\partial\phi_n}{\partial z} = K\phi_n, \text{ at } z = 0, \tag{6}$$

where $K = \omega^2/g$, and the boundary condition at the seabed

$$\frac{\partial\phi_n}{\partial z} = 0, \text{ at } z = -h. \tag{7}$$

The velocity potential should also satisfy the kinematic boundary condition at the n-th horizontal plate/membrane

$$\frac{\partial\phi_D}{\partial z} + \frac{\partial\phi_I}{\partial z} = \left.\frac{\partial\phi}{\partial z}\right|_{z=-d_n^{\pm}} = -\mathrm{i}p_nP_n(x) - \mathrm{i}\omega\eta_n, \text{ at } z = -d_n,\ |x-x_n| < a_n, \tag{8}$$

in which $P_n(x) = \phi|_{z=-d_n^-} - \phi|_{z=-d_n^+} = \phi_n^+ - \phi_n^-$ denotes the velocity potential jump across the n-th plane at $z = -d_n$, where $\phi_n^{\pm} = \phi_n|_{z=-d_n^{\mp}}$. Note that $P_n(x) = 0$ at $|x-x_n| > a_n$. Potential theory requires that $P_n(x) \sim C\sqrt{a_n^2 - (x-x_n)^2}$ as $|x-x_n| \to a_n$, in which C is x- independent. p_n denotes a complex porosity parameter when the plate/membrane is porous, where the real part corresponds to the resistance effect and the imaginary part corresponds to the inertial effect. The p_n term vanishes in the case of a nonpermeable plate or membrane. η_n represents the deflection of the plate/membrane. We have $\eta_n = 0$ in the case of a rigid plate.

The radiation boundary condition at $x \to \pm\infty$

$$\phi(x,z) \sim \begin{cases} \phi_I(x,z) + R\phi_I(-x,z), & x \to -\infty \\ T\phi_I(x,z), & x \to +\infty \end{cases} \tag{9}$$

should also be satisfied, where R and T are the complex reflection and transmission coefficients, respectively.

When the plate is flexible or a membrane, in addition to the above governing equation and boundary conditions, the dynamic boundary condition on the rectangular plate/membrane,

$$\mathrm{i}\omega P_n(x) = \begin{cases} g\left(-\chi_n \partial_{xxxx} + K\gamma_n\right)\eta_n, & \text{for an elastic plate} \\ g\left(\tau_n \partial_{xx} + K\gamma_n\right)\eta_n, & \text{for a membrane,} \end{cases} \tag{10}$$

should be satisfied (see e.g. [28, 15]). Here ∂_{xx} and ∂_{xxxx} represent second and fourth partial derivatives of a function with respect to x. χ_n denotes the flexural rigidity of the plate; γ_n represents the mass per unit length of the plate/membrane relative to the water density. τ_n represents the effect of equal uniform tension acting along the membrane, $\tau_n = T_n/(\rho g)$, where T_n denotes the initial membrane tension, and it is assumed that T_n is sufficiently large that dynamic tension effects may be neglected.

The edge boundary conditions of the plate/membrane must also be considered, affecting the expressions for η_n derived by using the dry mode expansion method. The expression of η_n will be given in Sec. 2.3.3.

2.2. Fourier transform and the inverse transform

Following Porter [6], we define the Fourier transform

$$\bar{\phi}_n(l,z) = \int_{-\infty}^{\infty} \phi_n(x,z)\mathrm{e}^{-\mathrm{i}lx}\mathrm{d}x, \tag{11}$$

with its inverse expressed as

$$\phi_n(x,z) = \frac{1}{2\pi}\int_{-\infty}^{\infty} \bar{\phi}_n(l,z)\mathrm{e}^{\mathrm{i}lx}\mathrm{d}l. \tag{12}$$

After performing the Fourier transform, the Laplace equation becomes

$$\left(\frac{\partial^2}{\partial z^2} - l^2\right)\bar{\phi}_n(l,z) = 0. \tag{13}$$

Similarly, after applying the Fourier Transform, the free surface boundary condition is

$$\frac{\partial \bar{\phi}_n(l,z)}{\partial z} = K\bar{\phi}_n(l,z), \quad z = 0, \tag{14}$$

the boundary condition at the seabed is

$$\frac{\partial \bar{\phi}_n(l,z)}{\partial z} = 0, \quad z = -h, \tag{15}$$

and the continuous velocity condition at the plane $z = -d_n$ is

$$\left.\frac{\partial \bar{\phi}_n(l,z)}{\partial z}\right|_{z=-d_n^-} = \left.\frac{\partial \bar{\phi}_n(l,z)}{\partial z}\right|_{z=-d_n^+}. \tag{16}$$

$P_n(x)$ can be converted into

$$\bar{P}_n(l) = \int_{-\infty}^{\infty} P_n(x)\mathrm{e}^{-\mathrm{i}lx}\mathrm{d}x = \int_{x_n-a_n}^{x_n+a_n} P_n(x)\mathrm{e}^{-\mathrm{i}lx}\mathrm{d}x = \bar{\phi}_n(l,-d_n^-) - \bar{\phi}_n(l,-d_n^+). \tag{17}$$

Solving Eq. (13) in $z \in [-d_n, 0]$ with (14) and in $z \in [-h, -d_n]$ with (15) and matching across $z = -d_n$ using Eqs. (16) and (17) gives

$$\bar{\phi}_n(l,z) = \bar{P}_n(l) f_n(l,z), \tag{18}$$

where

$$f_n(l,z) = \begin{cases} \dfrac{\sinh[l(h-d_n)][l\cosh(lz) + K\sinh(lz)]}{l\sinh(lh) - K\cosh(lh)}, & z \in [-d_n, 0], \\ \dfrac{\cosh[l(z+h)][-l\sinh(ld_n) + K\cosh(ld_n)]}{l\sinh(lh) - K\cosh(lh)}, & z \in [-h, -d_n]. \end{cases} \tag{19}$$

Taking the inverse transform of (18) in $z \in [-d_n, 0]$ using Eq. (12) gives

$$\phi_n(x,z) = \frac{1}{2\pi}\int_{-\infty}^{\infty} \frac{\bar{P}_n(l)\sinh[l(h-d_n)][l\cosh(lz) + K\sinh(lz)]}{l\sinh(lh) - K\cosh(lh)} \mathrm{e}^{\mathrm{i}lx}\mathrm{d}l. \tag{20}$$

This integral equation matches the form obtained by applying an integral transform representation of the Green's function. The introduced transform variable is key because performing the domain integral first keeps the equation well-behaved. Reversing this order produces hypersingular equations, which occur in thin plate problems and require specialised mathematical tools to solve (e.g., see [5]).

It should be noted from Eq. (20) that there are poles on the real axis at $l = \pm k$. To satisfy the radiation condition that ϕ_n is outgoing, the contour of integration is taken to pass over the pole at $l = -k$ and under the pole at $l = k$. Specifically, in $z \in [-d_n, 0]$, as we let $x \to \pm\infty$, we can deform the contour ϕ_m in Eq. (20) into either the upper-half or lower-half l-plane, capturing the residues at the poles $l = \pm k$, resulting in

$$\begin{aligned} \phi_n(x,z) &\sim \mathrm{i}\bar{P}_n(k)s_n(k)\cosh[k(z+h)]\mathrm{e}^{\mathrm{i}kx} \\ &= -\frac{\omega\cosh(kh)}{gA}\bar{P}_n(k)s_n(k)\phi_I(x,z), \quad x \to +\infty, \end{aligned} \tag{21}$$

and

$$\begin{aligned} \phi_n(x,z) &\sim -\mathrm{i}\bar{P}_n(-k)s_n(-k)\cosh[k(z+h)]\mathrm{e}^{-\mathrm{i}kx} \\ &= -\frac{\omega\cosh(kh)}{gA}\bar{P}_n(-k)s_n(k)\phi_I(-x,z), \quad x \to -\infty, \end{aligned} \tag{22}$$

where

$$s_n(\beta) = \left.\frac{(l-\beta)f_n(l,z)}{\cosh[k(z+h)]}\right|_{l\to\beta} \tag{23}$$

and

$$s_n(\pm k) = \frac{\sinh[k(h-d_n)]}{\pm 2hN_0} \quad \text{with} \quad N_0 = \frac{1}{2}\left(1 + \frac{\sinh(2kh)}{2kh}\right). \tag{24}$$

The equations derived here for the n-th plate/membrane are analogous to those Porter [6] developed for scattering by a single submerged rigid plate. Summing the contributions from all elements, the complex wave transmission and reflection coefficients T and R can now be expressed as

$$T = 1 - \frac{\omega\cosh(kh)}{gA}\sum_{n=1}^{N}\bar{P}_n(k)s_n(k), \tag{25}$$

and

$$R = -\frac{\omega\cosh(kh)}{gA}\sum_{n=1}^{N}\bar{P}_n(-k)s_n(k). \tag{26}$$

Therefore, after considering a real Cauchy principal-value integral and adding the contributions from the two poles, each contributing half of the residues, we obtain

$$\begin{aligned} \phi_D(x,z) = \frac{\mathrm{i}}{2}\cosh[k(z+h)]\sum_{n=1}^{N}[\bar{P}_n(k)\mathrm{e}^{\mathrm{i}kx} + \bar{P}_n(-k)\mathrm{e}^{-\mathrm{i}kx}]s_n(k) \\ + \frac{1}{2\pi}\sum_{n=1}^{N}\fint_{-\infty}^{\infty}\bar{P}_n(l)f_n(l,z)\mathrm{e}^{\mathrm{i}lx}\mathrm{d}l. \end{aligned} \tag{27}$$

Note that for $z \in [-d_n, 0]$, we have

$$\frac{\sinh[l(h-d_n)](l\cosh(lz)+K\sinh(lz))}{l\sinh(lh)-K\cosh(lh)} \sim \frac{1}{2}\mathrm{e}^{-|l|(z+d_n)}, \qquad |l| \to \infty. \tag{28}$$

As reported by Porter [6], an integral representation of the logarithm exists (see e.g. [29, §3.943]) for $z+d>0$

$$\ln\sqrt{(x-x')^2+(z+d)^2} = \frac{1}{2}\int_{-\infty}^{\infty}\frac{\mathrm{e}^{-|l|}-\mathrm{e}^{-|l|(z+d)}\mathrm{e}^{\mathrm{i}l(x-x')}}{|l|}\mathrm{d}l. \tag{29}$$

Hence, we have

$$\begin{aligned}\phi_n = {} & \frac{\mathrm{i}}{2}\cosh[k(z+h)][\bar{P}_n(k)\mathrm{e}^{\mathrm{i}kx}+\bar{P}_n(-k)\mathrm{e}^{-\mathrm{i}kx}]s_n(k) \\ & + \frac{1}{2\pi}\frac{\partial}{\partial z}\int_{x_n-a_n}^{x_n+a_n}P_n(x')\ln\sqrt{(x-x')^2+(z+d_n)^2}\mathrm{d}x' \\ & + \frac{1}{2\pi}\int_{-\infty}^{\infty}\left[\frac{\sinh[l(h-d_n)](l\cosh(lz)+K\sinh(lz))}{l\sinh(lh)-K\cosh(lh)}-\frac{1}{2}\mathrm{e}^{-|l|(z+d_n)}\right]\mathrm{e}^{\mathrm{i}lx}\bar{P}_n(l)\mathrm{d}l,\end{aligned} \tag{30}$$

for $z \in [-d_n, 0)$, and

$$\begin{aligned}\left.\frac{\partial\phi_n}{\partial z}\right|_{z=-d_n} = {} & \frac{\mathrm{i}}{2}k\sinh[k(h-d_n)][\bar{P}_n(k)\mathrm{e}^{\mathrm{i}kx}+\bar{P}_n(-k)\mathrm{e}^{-\mathrm{i}kx}]s_n(k) \\ & - \frac{1}{2\pi}\frac{\mathrm{d}^2}{\mathrm{d}x^2}\int_{x_n-a_n}^{x_n+a_n}P_n(x')\ln|x-x'|\mathrm{d}x' - \frac{1}{2\pi}\int_{-\infty}^{\infty}E_{n,n}(l)\mathrm{e}^{\mathrm{i}lx}\bar{P}_n(l)\mathrm{d}l,\end{aligned}$$

in which

$$\left(\frac{\partial^2}{\partial x^2}+\frac{\partial^2}{\partial z^2}\right)\ln\sqrt{(x-x')^2+(z+d)^2} = 0 \tag{31}$$

has been used to switch from z to x-derivatives, and

$$E_{n,n}(l) = \frac{l\sinh[l(h-d_n)][l\sinh(ld_n)-K\cosh(ld_n)]}{l\sinh(lh)-K\cosh(lh)} - \frac{1}{2}|l|. \tag{32}$$

Based on Eq. (27), and without applying the specialised logarithmic treatment indicated in Eq. (29), the velocity across the j-th plate/membrane level contributed by ϕ_n for $n \neq j$ can be expressed as

$$\left.\frac{\partial\phi_n}{\partial z}\right|_{z=-d_j} = \frac{\mathrm{i}}{2}k\sinh[k(h-d_j)][\bar{P}_n(k)\mathrm{e}^{\mathrm{i}kx}+\bar{P}_n(-k)\mathrm{e}^{-\mathrm{i}kx}]s_n(k) - \frac{1}{2\pi}\int_{-\infty}^{\infty}E_{n,j}(l)\mathrm{e}^{\mathrm{i}lx}\bar{P}_n(l)\mathrm{d}l, \tag{33}$$

where

$$E_{n,j}(l) = \begin{cases}\dfrac{l\sinh[l(h-d_n)](l\sinh(ld_j)-K\cosh(ld_j))}{l\sinh(lh)-K\cosh(lh)}, & d_j \leq d_n \\ \dfrac{l\sinh[l(h-d_j)](l\sinh(ld_n)-K\cosh(ld_n))}{l\sinh(lh)-K\cosh(lh)}, & d_j > d_n\end{cases} \tag{34}$$

2.3. Numerical method

Determination of the potential jump across the structures represents a key step in our analysis. For flexible structures such as elastic plates and membranes, the deformation is an additional unknown. However, this can be resolved through the dynamic boundary condition, i.e., Eq. (10), which couples the structural deflection directly to the potential jump. Once this jump is solved for, then derived quantities–including the wave reflection/transmission coefficients, hydrodynamic forces, and structural deflection–readily follow.

In this subsection, following the strategy developed by Porter [6] and introduced by Parsons & Martin [5] among others, we obtain an accurate and efficient approximate solution using a variational approach

(Galerkin's method). The unknown potential jump is expanded in an orthogonal basis that inherently captures the expected square-root behaviour in the pressure distribution at the edges of the plates or membranes.

2.3.1. Potential jump across the plate/membrane

Employing the Galerkin approximation method, the unknown potential jump function across the nth plate/membrane is expanded as

$$P_n(x) = \sum_{p=0}^{\infty} \alpha_{n,p} w_p\left(\frac{x - x_n}{a_n}\right), \quad \text{with} \quad w_p(u) = \frac{\mathrm{i}^p \sqrt{1-u^2}}{(p+1)\pi} U_p(u), \tag{35}$$

where $U_p(u)$ are Chebyshev polynomials of the second kind having a square-root behaviour at $u = \pm 1$ and the orthogonal property with respect to the weight $\sqrt{1-u^2}$ (see e.g. [29, §7.34])

$$\int_{-1}^{1} \sqrt{1-u^2} U_p(u) U_q(u) \mathrm{d}u = \frac{\delta_{p,q}\pi}{2}. \tag{36}$$

After inserting Eq. (35) into Eq. (17), along with relevant properties of the second-kind Chebyshev polynomials $U_p(u)$ as shown in Eq. (A.2), $\bar{P}_n(l)$ can be expressed in terms of $\alpha_{n,p}$ as

$$\bar{P}_n(l) = \int_{-\infty}^{\infty} P_n(x) \mathrm{e}^{-\mathrm{i}lx} \mathrm{d}x = \int_{x_n - a_n}^{x_n + a_n} P_n(x) \mathrm{e}^{-\mathrm{i}lx} \mathrm{d}x = \frac{\mathrm{e}^{-\mathrm{i}lx_n}}{l} \sum_{p=0}^{\infty} \alpha_{n,p} \mathrm{J}_{p+1}(la_n). \tag{37}$$

2.3.2. Rigid plate

For a fixed rigid plate, we have $\eta_j = 0$ in Eq. (8). After imposing the plate boundary condition on $z = -d_j$, i.e., inserting Eq. (27) into Eq. (8) with $\eta_j = 0$, we have

$$\begin{aligned} &\mathrm{i}p_j P_j(x) + \frac{\mathrm{i}}{2} k \sinh[k(h-d_j)] \sum_{n=1}^{N} [\bar{P}_n(k) \mathrm{e}^{\mathrm{i}kx} + \bar{P}_n(-k) \mathrm{e}^{-\mathrm{i}kx}] s_n(k) \\ &- \frac{1}{2\pi} \frac{\mathrm{d}^2}{\mathrm{d}x^2} \int_{x_j - a_j}^{x_j + a_j} P_j(x') \ln|x - x'| \mathrm{d}x' - \frac{1}{2\pi} \int_{-\infty}^{\infty} \sum_{n=1}^{N} E_{n,j}(l) \mathrm{e}^{\mathrm{i}lx} \bar{P}_n(l) \mathrm{d}l \\ =& \frac{\mathrm{i}gkA \sinh[k(h-d_j)] \mathrm{e}^{\mathrm{i}kx}}{\omega \cosh(kh)}, \end{aligned} \tag{38}$$

and after further multiplying both sides of the above equation by $w^*_{p'}((x - x_j)/a_j)$ for $p' = 0, 1, 2, \cdots$, integrating over the interval $|x - x_j| < a_j$, employing expressions of the potential jump $P_n(x)$ and its Fourier transform $\bar{P}_n(l)$, i.e., Eqs. (35) and (37), along with relevant properties of the second-kind Chebyshev polynomials $U_p(u)$ as shown in Eqs. (A.3)-(A.6), and rearranging accordingly, we obtain

$$\begin{aligned} &\mathrm{i}p_j a_j \sum_{p=0}^{\infty} \alpha_{j,p} \frac{\mathrm{i}^{p-p'} U_{p,p'}}{(p+1)(p'+1)\pi^2} - \frac{1}{4\pi(p'+1)} \alpha_{j,p'} - \frac{1}{2\pi} \sum_{n=1}^{N} \sum_{p=0}^{\infty} \alpha_{n,p} K_{n,j,p,p'} \\ &+ \frac{\mathrm{i}}{2k} \sinh[k(h-d_j)] \mathrm{J}_{p'+1}(ka_j) \sum_{n=1}^{N} \sum_{p=0}^{\infty} \alpha_{n,p} \mathrm{J}_{p+1}(ka_n) [\mathrm{e}^{-\mathrm{i}k(x_n - x_j)} + (-1)^{p+p'} \mathrm{e}^{\mathrm{i}k(x_n - x_j)}] s_n(k) \\ =& \frac{\mathrm{i}gA \sinh[k(h-d_j)] \mathrm{e}^{\mathrm{i}kx_j} \mathrm{J}_{p'+1}(ka_j)}{\omega \cosh(kh)}, \end{aligned} \tag{39}$$

where

$$K_{n,j,p,p'} = \int_{-\infty}^{\infty} E_{n,j}(l) \frac{\mathrm{e}^{-\mathrm{i}l(x_n - x_j)} \mathrm{J}_{p+1}(la_n) \mathrm{J}_{p'+1}(la_j)}{l^2} \mathrm{d}l, \tag{40}$$

which can be evaluated numerically through Gaussian quadrature. The required number of quadrature points generally scales with the magnitude of the wavenumbers to maintain precision.

The unknown coefficients $\alpha_{n,p}$ can be determined by solving a linear algebraic system, i.e., Eq. (39), after truncation.

2.3.3. Simply supported flexible plate/membrane

For simply supported edge conditions, the deformation of the nth plate/membrane can be expressed as

$$\eta_n(x) = \sum_{m=1}^{\infty} w_{n,m} \sin\left[\frac{m\pi(x + a_n - x_n)}{2a_n}\right], \tag{41}$$

where $w_{n,m}$ are unknown coefficients to be determined. The present model can be easily extended to plate/membrane with other edge conditions, such as clamped edges, for which the corresponding expression for the deformation η_n is different. For brevity, only cases involving simply supported edge conditions are presented in this paper.

After inserting the expressions for $\eta_j(x)$ (Eq. (41)) and $P_j(x)$ (Eq. (35)) into Eq. (10), multiplying both sides by $\sin\left(m'\pi(x + a_j - x_j)/(2a_j)\right)/a_j$ for $m' = 1, 2, \cdots$, integrating over $|x - x_j| < a_j$, and rearranging, $w_{j,m'}$ can be expressed in terms of $\alpha_{j,p}$ as follows

$$w_{j,m'} = \mathrm{i}\omega \sum_{p=0}^{\infty} \frac{V_{p,m'}\alpha_{j,p}}{T^{(\zeta)}_{j,m'}}, \tag{42}$$

where

$$\begin{aligned} V_{p,m'} &= \frac{1}{a_j}\int_{x_j - a_j}^{x_j + a_j} w_p\left(\frac{x - x_j}{a_j}\right) \sin\left[\frac{m'\pi(x + a_j - x_j)}{2a_j}\right] \mathrm{d}x \\ &= \begin{cases} \dfrac{2(-\mathrm{i})^{m'-1}}{m'\pi} \mathrm{J}_{p+1}\left(\dfrac{m'\pi}{2}\right), & (m' + p) \text{ is odd} \\ 0, & (m' + p) \text{ is even,} \end{cases} \end{aligned} \tag{43}$$

and

$$T^{(\zeta)}_{j,m'} = \begin{cases} g\left[-\chi_j\left(\dfrac{m'\pi}{2a_j}\right)^4 + K\gamma_j\right], & \zeta = 1 \\ g\left[-\tau_j\left(\dfrac{m'\pi}{2a_j}\right)^2 + K\gamma_j\right], & \zeta = 2, \end{cases} \tag{44}$$

in which $\zeta = 1, 2$ represent the elastic plate and membrane cases, respectively.

For a flexible plate/membrane, the effect of its structural deformation on the kinematic boundary condition (in terms of $\mathrm{i}\omega\eta_j$, see Eq. (39)) should be taken into consideration. Hence, employing Eq. (42), the term,

$$-\omega^2 a_j \sum_{m=1}^{\infty}\sum_{p=0}^{\infty} \frac{V_{p,m}V^*_{p',m}}{T^{(\zeta)}_{j,m}}\alpha_{j,p}, \tag{45}$$

should be added to the LHS of Eq. (39).

2.4. Wave power dissipation

Wave power is dissipated as the water flows across porous plates/membranes. In such cases, the wave power dissipated by the plates/membranes may be calculated by [30]

$$P_{diss} = \frac{\rho\omega}{2}\sum_{n=1}^{N}\int_{x_n-a_n}^{x_n+a_n}\mathrm{Re}(p_n)|P_n(x)|^2\mathrm{d}x. \tag{46}$$

In addition to the direct approach, wave power dissipation can be predicted using the energy conservation principle, whereby the dissipated wave power is the difference between the incident wave power and that reflected from and transmitted after the plate/membrane. As $x \to \pm\infty$ we have

$$\frac{\partial\phi(x,y,z)}{\partial x} \sim \begin{cases} \mathrm{i}k\phi_I(x,z) - \mathrm{i}k\phi_I(-x,z)R, & x \to -\infty \\ \mathrm{i}k\phi_I(x,z)T, & x \to +\infty \end{cases} \tag{47}$$

and

$$\begin{aligned} P_{diss} =& -\int_{-h}^{0}\frac{1}{2}\mathrm{Re}\left\{\mathrm{i}\omega\rho\left[\left(\phi\frac{\partial\phi^*}{\partial x}\right)\Big|_{x=+\infty} - \left(\phi\frac{\partial\phi^*}{\partial x}\right)\Big|_{x=-\infty}\right]\right\}\mathrm{d}z \\ =& \frac{\omega\rho}{2}\int_{-h}^{0}\mathrm{Im}\left\{\left(\phi\frac{\partial\phi^*}{\partial x}\right)\Big|_{x=+\infty} - \left(\phi\frac{\partial\phi^*}{\partial x}\right)\Big|_{x=-\infty}\right\}\mathrm{d}z \\ =& \mathcal{P}_{in}\left[1 - \left(|T|^2 + |R|^2\right)\right], \end{aligned} \tag{48}$$

in which $\mathcal{P}_{in}$ represents the incoming wave power per unit width of the wave front,

$$\mathcal{P}_{in} = \frac{\omega\rho k}{2}\int_{-h}^{0}|\phi_I|^2\mathrm{d}z = \frac{\rho g A^2}{2}\frac{\omega}{2k}\left[1 + \frac{2kh}{\sinh(2kh)}\right]. \tag{49}$$

The wave power capture efficiency of the plate/membrane may be expressed as

$$\eta_{diss} = \frac{P_{diss}}{\mathcal{P}_{in}} = 1 - \left(|T|^2 + |R|^2\right). \tag{50}$$

2.5. Free surface elevation

After inserting the expression of ϕ into $\eta = \mathrm{i}\omega\phi|_{z=0}/g$, the free surface elevation is given by

$$\begin{aligned} \eta &= A\mathrm{e}^{\mathrm{i}kx} + \frac{\mathrm{i}\omega}{g}\phi_D|_{z=0} \\ &= A\mathrm{e}^{\mathrm{i}kx} - \frac{\omega\cosh(kh)}{2kg}\sum_{n=1}^{N}\sum_{p=0}^{\infty}\alpha_{n,p}\mathrm{J}_{p+1}(a_n k)[\mathrm{e}^{\mathrm{i}k(x-x_n)} + (-1)^p\mathrm{e}^{-\mathrm{i}k(x-x_n)}]s_n(k) \\ &+ \frac{\mathrm{i}\omega}{2\pi g}\sum_{n=1}^{N}\sum_{p=0}^{\infty}\alpha_{n,p}\int_{-\infty}^{\infty}\frac{\sinh[l(h-d_n)]}{l\sinh(lh) - K\cosh(lh)}\mathrm{J}_{p+1}(a_n l)\mathrm{e}^{\mathrm{i}l(x-x_n)}\mathrm{d}l. \end{aligned} \tag{51}$$

2.6. Wave forces and wave moments

On integrating the pressure jump across the structure over the whole of the nth plate/membrane, the wave force is expressed as

$$F_n = -\mathrm{i}\omega\rho\int_{x_n-a_n}^{x_n+a_n}P_n(x)\mathrm{d}x = -\frac{\mathrm{i}\omega\rho a_n\alpha_{n,0}}{2}. \tag{52}$$

Similarly, the wave-induced wave moment acting on the nth plate/membrane about its centre can be calculated with

$$M_n = \mathrm{i}\omega\rho \int_{x_n-a_n}^{x_n+a_n} P_n(x)(x-x_n)\mathrm{d}x = \frac{-\omega\rho a_n^2 \alpha_{n,1}}{8}. \tag{53}$$

The coefficients $\bar{F}_n$ and $\bar{M}_n$, defined as

$$\bar{F}_n = \frac{|F_n|}{2\rho g a_n A}; \quad \text{and} \quad \bar{M}_n = \frac{|M_n|}{4\rho g a_n^2 A} \tag{54}$$

are introduced to nondimensionalise the wave-induced forces and moments.

3. Convergence analysis and model verification

Figure 2 shows the effect of the two numerical cut-off parameters–p_0 for the potential jump function ($p = 0, 1, 2, \cdots, p_0$) and m_0 for the dry plate modes ($m = 1, 2, \cdots, m_0$)–on the calculated wave power dissipation for dual submerged horizontal porous flexible plates. Converged results are achieved for $p_0 > 5$ and $m_0 > 3$. Consequently, the values $p_0 = 10$ and $m_0 = 10$ are adopted for all subsequent analyses.

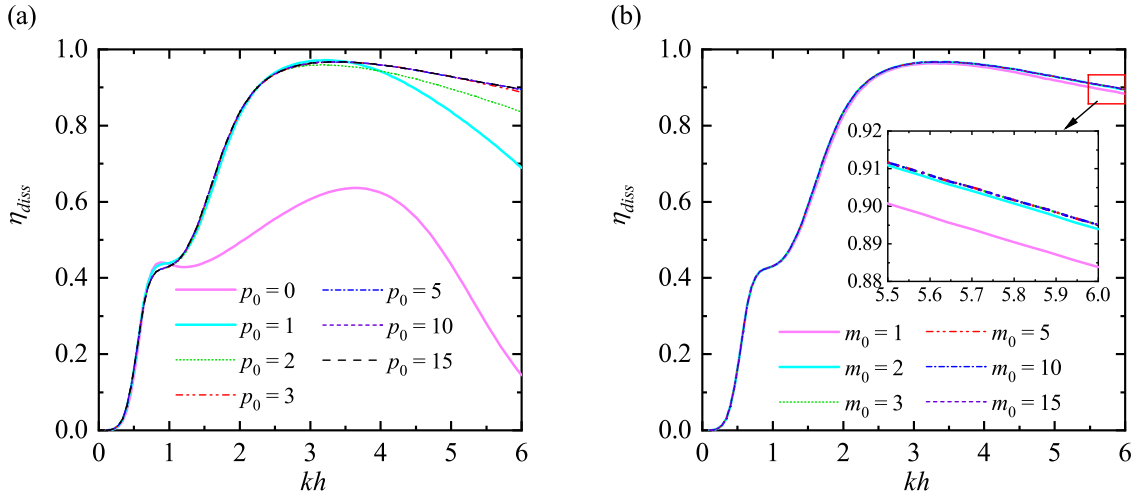

Figure 2: Impact of two types of cut-offs on the wave power dissipation coefficients for dual submerged horizontal porous flexible plates: (a) the cut-off (p_0) for the potential jump function across the structure, with m_0 fixed at 10; and (b) the cut-off (m_0) for the dry modes of plate deflection, with p_0 fixed at 10. The system parameters are $N = 2$, $x_1 = 0$, $x_2/h = 0.25$, $a_1/h = a_2/h = 0.5$, $d_1/h = 0.12$, $d_2/h = 0.18$, $\chi_1/h^4 = \chi_2/h^4 = 0.01$, $\gamma_1/h = \gamma_2/h = 0.01$, and $2\pi p_1/k = 2\pi p_2/k = 5.0$.

For verification purposes, the present wave model is tested for three benchmark wave-interaction problems involving: (1) a single impermeable flexible membrane/plate (Fig. 3), (2) dual coaxial porous rigid plates (Fig. 4), and (3) dual staggered porous flexible plates (Fig. 5). The predictions by the present model are in excellent agreement with results from a previously validated model based on the boundary element method (BEM) [12, 24] and results from other theoretical models based on eigenfunction matching [13, 19], thus verifying the present theoretical model of wave scattering by multiple submerged horizontal plates or membranes.

In the case of dual staggered porous flexible plates, switching the horizontal positions of the two plates alters the wave power dissipation and reflection coefficients of the system (see Fig. 5). Interestingly, the

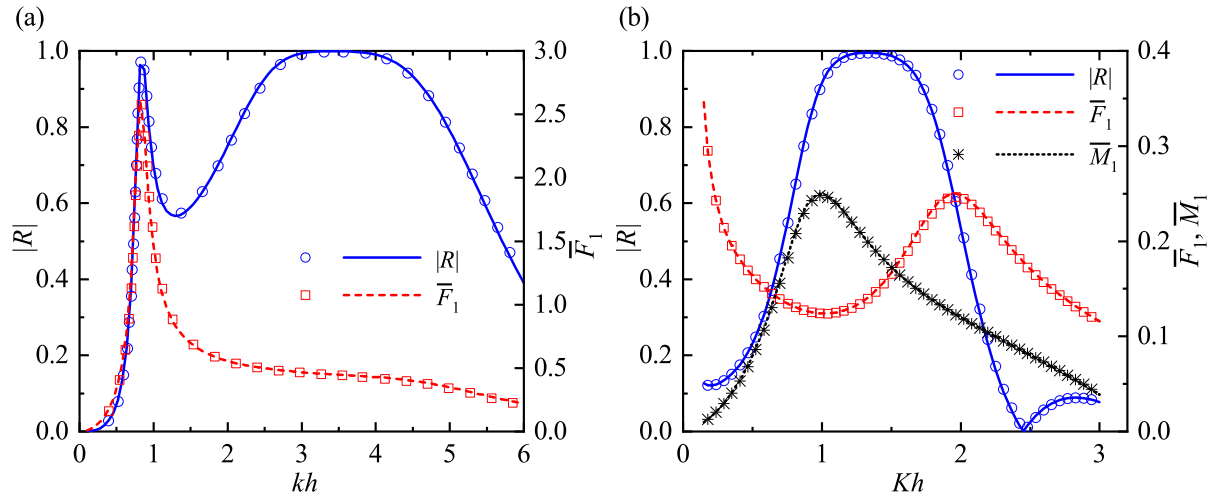

Figure 3: Frequency response of the reflection coefficients and wave force coefficients for: (a) a flexible membrane with $a_1/h = 0.5$, $d_1/h = 0.2$, $p_1 = 0$, $\tau_1/h^2 = 0.1$, and $\gamma_1/h = 0.001$; (b) a flexible plate with $a_1/h = 4/3$, $d_1/h = 1/3$, $p_1 = 0$, $\chi_1/h^4 = (2/3)^4$, and $\gamma_1/h = 1/15$. Lines show the present results, whereas the symbols in Fig. 3a denote the analytical results by using a natural mode expansion-based eigenfunction matching method [12], and the symbols in Fig. 3b represent alternative analytical results derived via a dispersion relation-based eigenfunction matching method, following the approach of [13].

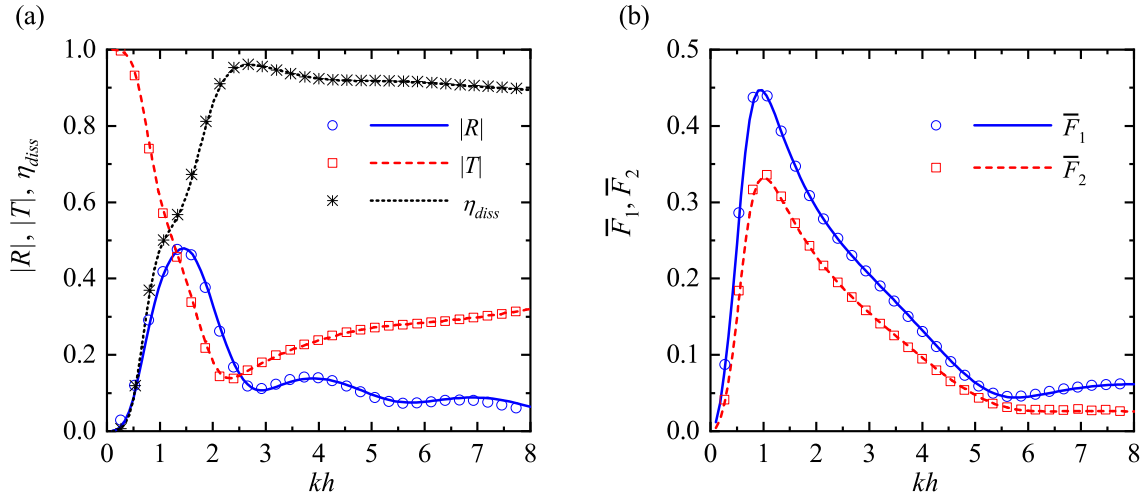

Figure 4: Frequency response of the reflection coefficients, transmission coefficients, wave power dissipation coefficients, and wave force coefficients for dual submerged horizontal porous plates with $x_1 = x_2$, $a_1/h = a_2/h = 0.5$, $d_1/h = 0.1$, $d_2/h = 0.2$, and $2\pi p_1/k = 2\pi p_2/k = 5.0$: (a) $|R|$, $|T|$, and η_{diss}; (b) $\bar{F}_1$ and $\bar{F}_2$. Lines show the present results and symbols indicate the multi-domain BEM numerical results from [24].

wave transmission coefficient remains constant across all wave frequencies. The present model provides a theoretical explanation for this transmission invariance; the detailed proof is given in Appendix B. As expected, predictions by direct and indirect approaches of wave power dissipation by the dual porous flexible plates are in strong agreement. Figure 6 illustrates the displacements of the water surface and dual staggered porous flexible plates at $kh = 3.0$. The incident wave amplitude is $0.05h$ for visual clarity. For these wave conditions, the dual porous flexible plates exhibit effective wave power dissipation and attenuation.

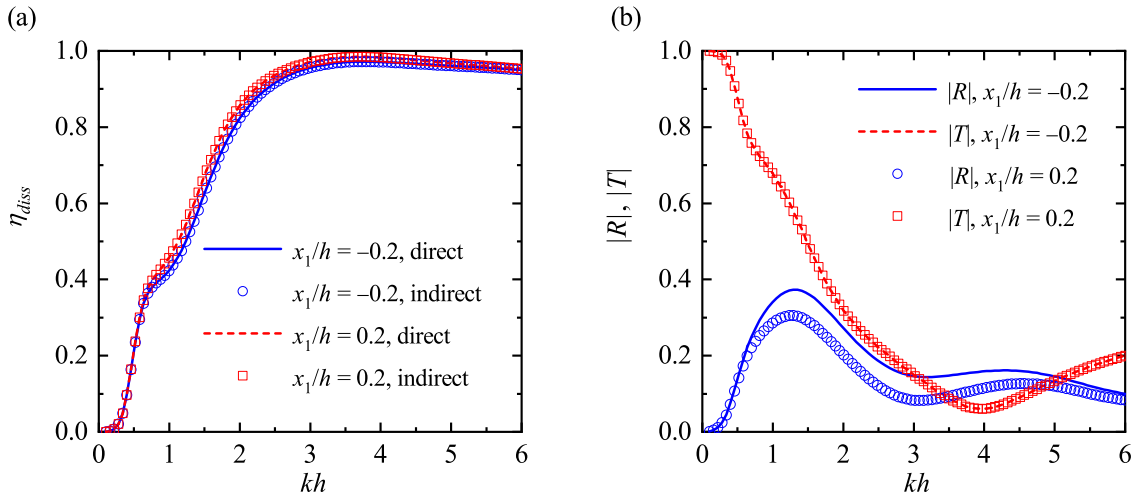

Figure 5: Frequency response of the wave power dissipation coefficients, reflection coefficient, and transmission coefficients for dual submerged horizontal porous flexible plates with $x_1 = -x_2$, $a_1/h = a_2/h = 0.5$, $d_1/h = 0.1$, $d_2/h = 0.2$, $\chi_1/h^4 = \chi_2/h^4 = 0.01$, and $\gamma_1/h = \gamma_2/h = 0.01$, and $2\pi p_1/k = 2\pi p_2/k = 5.0$: (a) η_{diss}; (b) $|R|$ and $|T|$. In Fig. 5, the lines and symbols respectively show the wave power dissipation predicted by the direct and indirect methods, i.e., Eqs. (46) and (48).

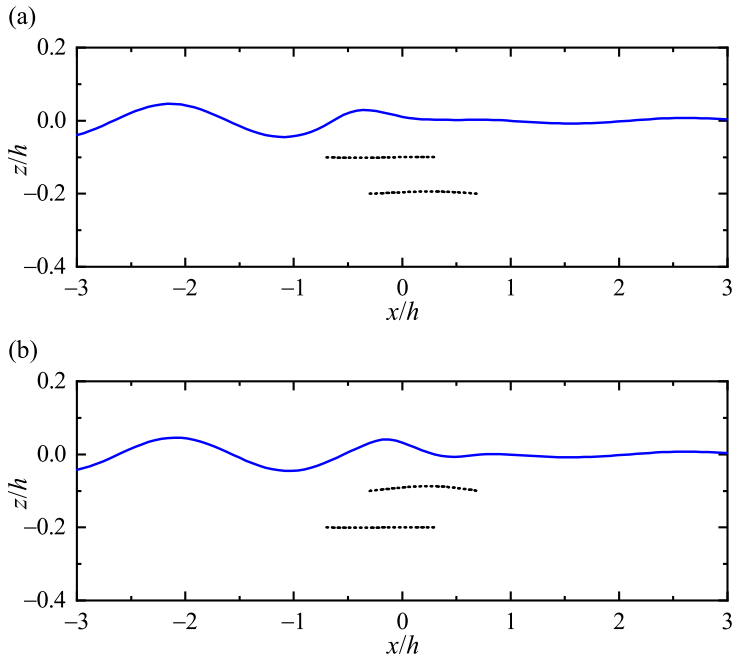

Figure 6: Water surface and plate displacements for wave scattering by dual submerged horizontal porous flexible plates with $x_1 = -x_2$, $a_1/h = a_2/h = 0.5$, $d_1/h = 0.1$, $d_2/h = 0.2$, $\chi_1/h^4 = \chi_2/h^4 = 0.01$, and $\gamma_1/h = \gamma_2/h = 0.01$, and $2\pi p_1/k = 2\pi p_2/k = 5.0$, $kh = 3.0$, $t = 0$: (a) $x_1/h = -0.2$; (b) $x_1/h = 0.2$.

4. Results and discussion

4.1. Dual porous flexible plates

Using our theoretical model, we investigate the influence of relative horizontal and vertical positions and the length ratio of dual porous flexible plates on wave reflection/transmission coefficients, wave power

dissipation, and the wave excitation forces and moments experienced by each plate. The physical parameters of the two plates are fixed as follows: $\chi_1/h^4 = \chi_2/h^4 = 0.01$, $\gamma_1/h = \gamma_2/h = 0.01$, $2\pi p_1/k = 2\pi p_2/k = 5.0$. Unless otherwise specified, the geometrical parameters, including location, are $x_1/h = -0.75$, $x_2/h = 0.75$, $a_1/h = a_2/h = 0.5$, $d_1/h = 0.1$, $d_2/h = 0.2$.

4.1.1. Effect of relative horizontal position of plates

To analyse the effect of horizontal position, Plate 1 is fixed at $x_1/h = 0$, whereas the position of Plate 2 is varied such that x_2/h ranges from -1.5 to 1.5. This range encompasses three deployment configurations: coaxial ($x_2/h = 0$), staggered ($0 < |x_2|/h < 1.0$), and side-by-side ($|x_2|/h > 1.0$).

Figure 7 displays the frequency responses of the wave reflection coefficient $|R|$, wave transmission coefficient $|T|$, and the power dissipation coefficient η_{diss} for different relative horizontal positions of the plates. When deployed coaxially ($x_2/h = 0$), the reflection coefficient ($|R|$) of the system as a function of kh contains two distinct peaks (see Fig. 7a). A primary peak occurs near $kh = 1.5$ ($|R| = 0.46$), and a secondary peak appears at $kh = 4.7$ ($|R| = 0.18$). When Plate 2 shifts seaward to $x_2/h = -0.5$, both peaks migrate toward lower frequencies. The amplitude of the main peak decreases significantly from $|R| = 0.46$ to 0.27, whereas that of the secondary peak increases slightly. When Plate 2 shifts further seaward to $x_2/h = -1.0$ and -1.5, both peaks continue migrating toward progressively lower frequencies, and new peaks emerge within the simulated wave frequency range. Analogous behaviour in the position and multiplicity of peaks occurs when Plate 2 shifts leeward from $x_2/h = 0$ to 1.0 and 1.5, mirroring the seaward displacement pattern. Figure 7b further demonstrates the invariance of the transmission coefficient $|R|$ to swapped horizontal positions of Plates 1 and 2, despite variations in both $|R|$ and η_{diss} as plotted in Fig. 7a and 7c. The invariance of transmission to plate order, despite changes in reflection and dissipation, stems from the linear, reciprocal nature of wave propagation. The total transmission coefficient represents the net effect of a wave traversing the entire structure. While swapping plates alters the local interference governing reflection and energy loss at each stage, the principle of reciprocity suggests the cumulative attenuation and phase shift for a forward-travelling wave can remain unchanged. This implies the two-plate system functions as a composite 'black box' with an intrinsic transmittance. Consequently, designers can treat transmission as a property of the plate pair, whereas reflection and dissipation require specific optimisation of the sequence. This result aligns with our previous work [31], which demonstrated that a given 2D raft-type wave energy converter possesses a unique transmission coefficient, unaffected by whether waves approach from the front or rear. The wave transmission coefficient $|T|$ is insensitive to changes in x_2/h near $kh \approx 1.6$. At this frequency, staggered or side-by-side plate configurations dissipate more wave power than coaxial arrangements. For $kh > 3.0$, staggered or side-by-side plate configurations outperform coaxial deployments in wave attenuation. At $kh = 4.6$, minimal wave transmission occurs behind the plates ($|T| \approx 0$) when $x_2/h = \pm 1.0$.

Figure 8a shows that the wave force on Plate 1 increases in long incident waves ($kh < 0.70$) when the configuration is changed from coaxial to either staggered or side-by-side, regardless as to whether Plate 2 is positioned on the seaward or leeward of Plate 1. A similar trend is observed for the wave force on Plate 2 under $kh < 0.52$, as shown in Fig. 8b. Generally, for $kh > 1.5$, the seaward plate experiences significantly

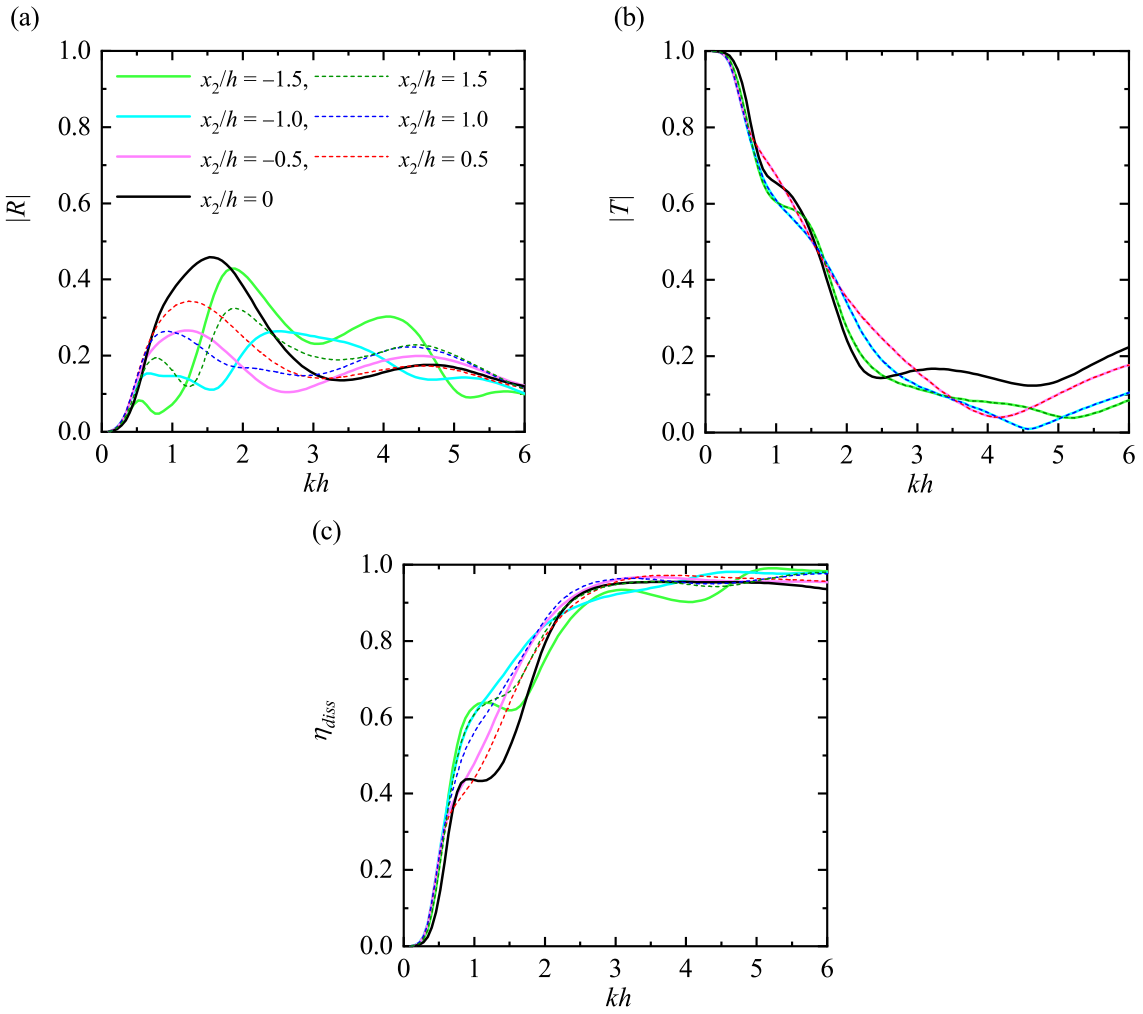

Figure 7: Frequency response of reflection coefficients, transmission coefficients, and wave power dissipation coefficients of dual submerged horizontal porous flexible plates for $x_1 = 0$, $a_1/h = a_2/h = 0.5$, $d_1/h = 0.1$, $d_2/h = 0.2$, and different relative horizontal positions of Plate 2 in terms of x_2 ranging between $-1.5h$ to $1.5h$: (a) $|R|$; (b) $|T|$; and (c) η_{diss}.

larger wave forces and moments than for a coaxial arrangement, while the leeward plate experiences smaller forces and moments. However, exceptions occur; for example, at $kh = 2.0$ with a staggered configuration ($x_2/h = \pm 0.5$), both $\bar{M}_1$ and $\bar{M}_2$ are smaller than their coaxial counterparts. As kh increases from 0.5 to 6.0, the wave-induced force and moment on the seaward plate exhibit oscillatory behaviour. The oscillation frequency increases with distance between the plates. This phenomenon arises because the incident waves and the waves reflected from the leeward plate simultaneously interact with the seaward plate. Variations in wave frequency alter the phase difference, leading to periodic amplification and reduction of the resulting forces and moments, i.e., an oscillatory response.

4.1.2. Effect of relative vertical position between plate

We examine dual side-by-side porous flexible plates positioned at $x_1/h = -0.75$, $x_2/h = 0.75$ with combined draft $d_1/h + d_2/h = 0.3$. Figures 9 and 10 show frequency responses of $|R|$, $|T|$, η_{diss}, and wave-induced forces and moments for d_1/d_2 ratio ranging from 1/2 to 2/1. The influence of d_1/d_2 on $|R|$

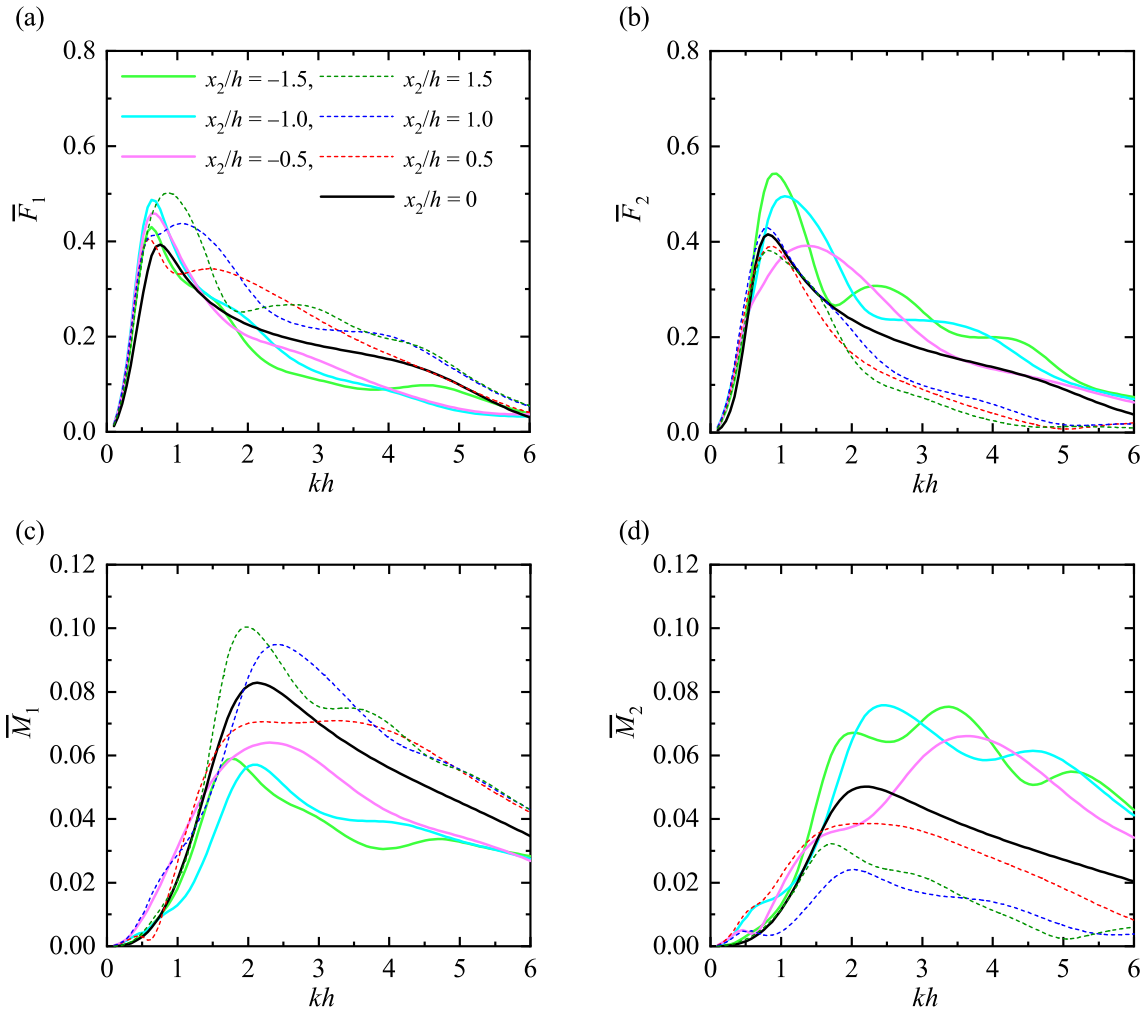

Figure 8: Frequency response of the wave-induced forces and moments on dual submerged horizontal porous flexible plates for $x_1 = 0$, $a_1/h = a_2/h = 0.5$, $d_1/h = 0.1$, $d_2/h = 0.2$, and different relative horizontal positions of Plate 2 in terms of x_2 ranging between $-1.5h$ to $1.5h$: (a) $\bar{F}_1$; (b) $\bar{F}_2$; (c) $\bar{M}_1$; and (d) $\bar{M}_2$.

reverses across wave frequencies: near $kh = 0.75$ and $kh = 5.40$, a smaller seaward plate draft enhances wave reflection, whereas it reduces reflection near $kh = 3.75$. The transmission coefficient $|T|$ remains invariant when plate submergence ratios are interchanged (Fig. 9b). While d_1/d_2 variation minimally affects $|T|$ in long waves ($kh < 2.0$), increased submergence disparity reduces $|T|$ for $kh > 4.5$. Mid-frequency waves ($1.5 < kh < 4.5$) exhibit peak dissipation when the seaward plate has a shallower draft.

The wave-induced forces and moments on a plate in the dual-plate system generally increase with reduced submergence, especially in long waves (Fig. 10). However, exceptions occur–e.g., at $kh \approx 1.2$, where $\bar{F}_2$ is larger when Plate 2 has greater submergence.

4.1.3. Effect of length ratio

Figures 11 and 12 display the effect of length ratio (a_1/a_2) on the response of coaxial plates ($x_1 = x_2 = 0$) of fixed total length $a_1/h + a_2/h = 1.0$ and two values of draft, $d_1/h = 0.1$ and $d_2/h = 0.2$. For equal lengths ($a_1/h = a_2/h = 0.5$), $|R|$ exhibits bimodality, with a primary peak ($|R| = 0.46$ at $kh = 1.53$) and a

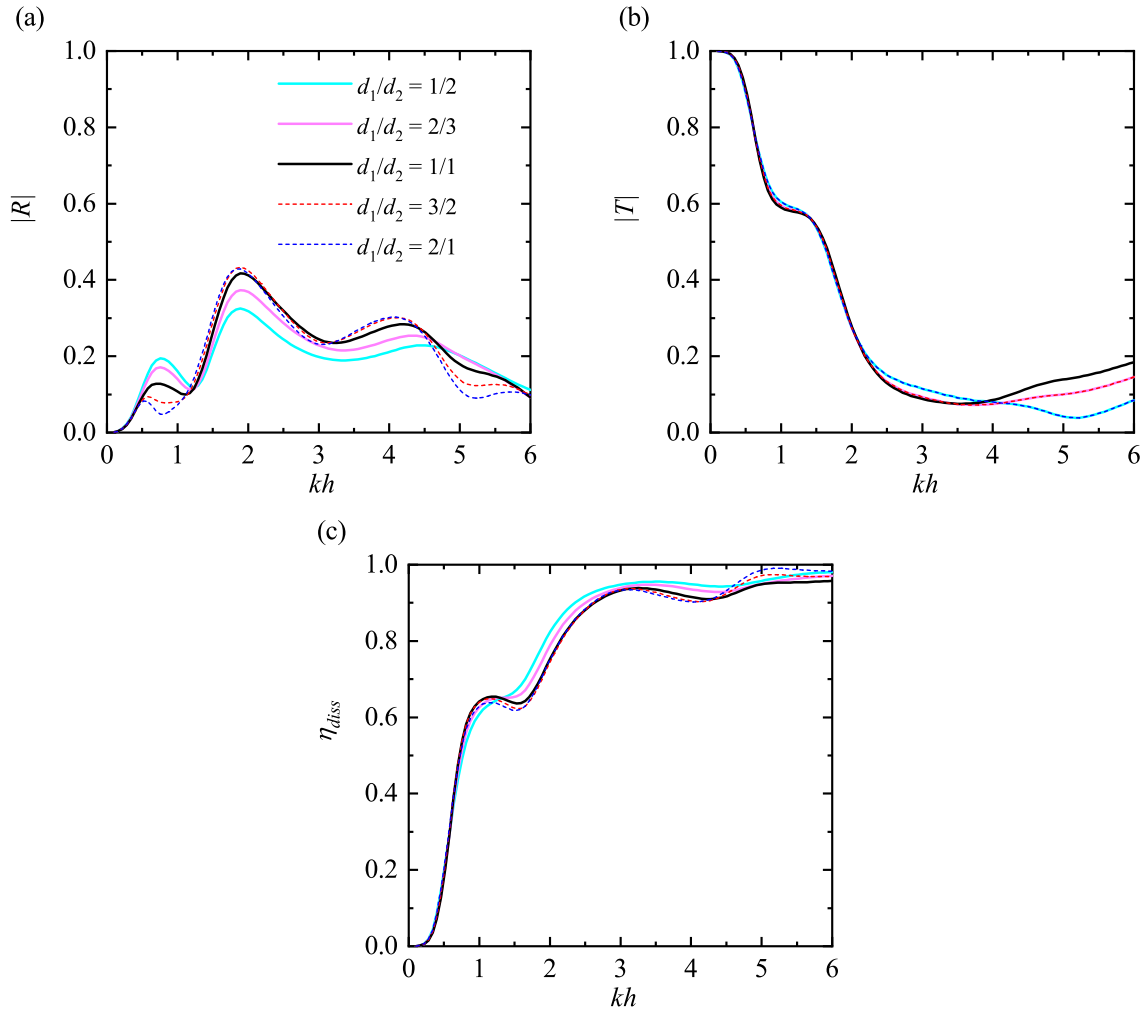

Figure 9: Frequency response of reflection coefficient, transmission coefficients, and wave power dissipation coefficients of dual submerged horizontal porous flexible plates for $x_1/h = -0.75$, $x_2/h = 0.75$, $a_1/h = a_2/h = 0.5$, $d_1/h + d_2/h = 0.3$, and different relative vertical positions of the two plates in terms of d_1/d_2 ranging between 1/2 to 2/1: (a) $|R|$; (b) $|T|$; and (c) η_{diss}.

secondary peak ($|R| = 0.18$ near $kh = 4.69$). Reducing a_1/a_2 to 1/2 suppresses $|R|$ across $0.5 < kh < 6.0$. Further reduction to 1/3 enhances suppression over $0.5 < kh < 3.5$, achieving near-total wave dissipation at $kh = 3.0$ ($|R|$ and $|T| \approx 0$). At $kh > 5.0$, progressive increase in the length of Plate 1 in the coaxial system improves wave attenuation (lower $|T|$) and boosts wave power dissipation. This occurs because the energy of short waves concentrates near the free surface, and a longer Plate 1 at shallower draft intercepts more wave power, thereby enhancing dissipation and reducing wave transmission behind the plates.

As shown in Fig. 12, the wave-induced forces and moments increase with plate length in long waves ($kh < 0.22$), regardless of submergence depth, and scale with kh. The wave-induced forces and moments decay with further increase in kh after reaching a peak value. The peak occurrence shifts to lower kh for longer plates. Notably, for $1.0 < kh < 2.5$, Plate 1 for $a_1/a_2 = 3/1$ exhibits the smallest $|F_1|$ despite being the longest among the five examined cases with different length ratios. This stems from half-wavelength resonance, whereby opposing vertical forces develop along the plate (phase cancellation), minimising net force while

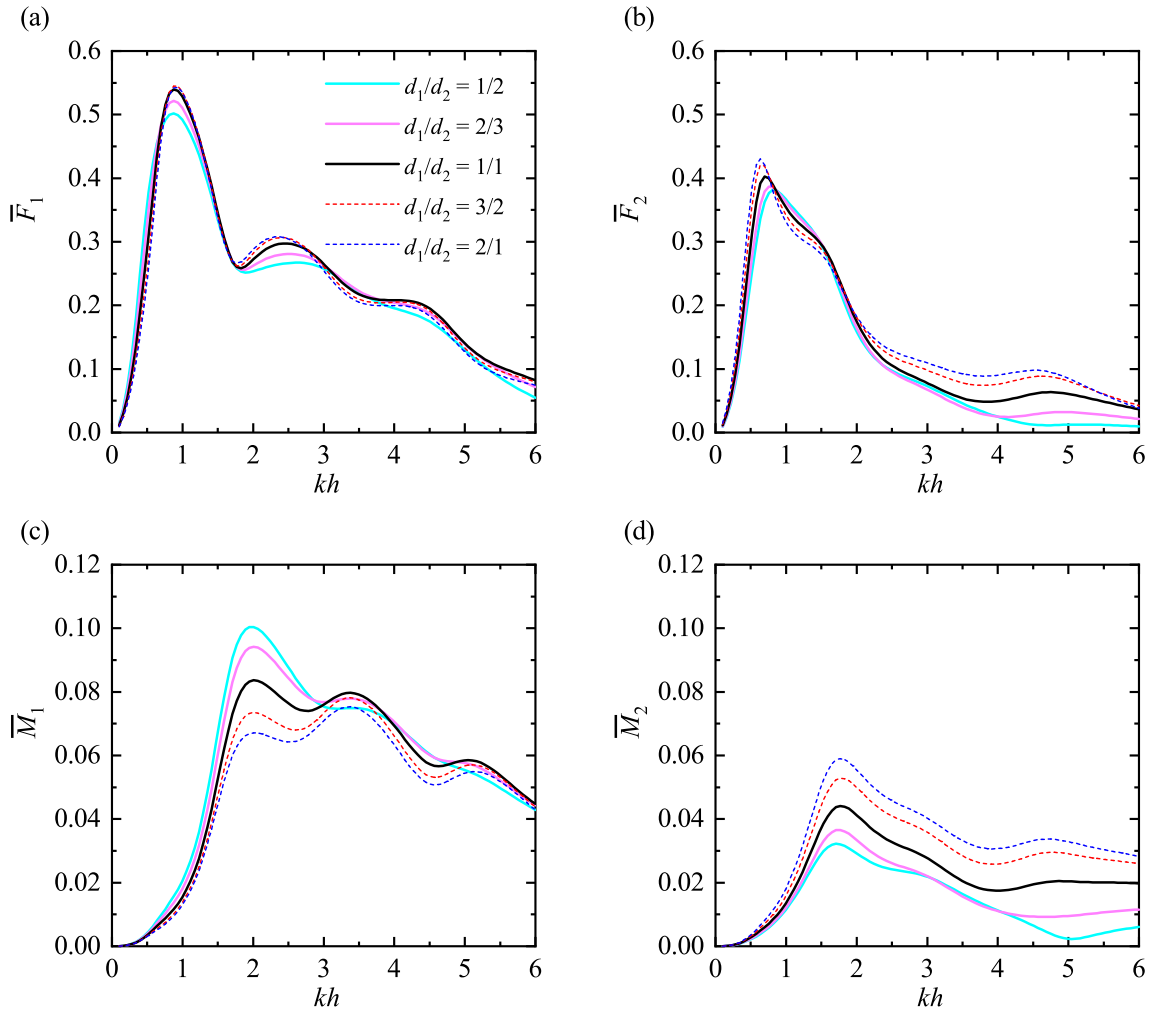

Figure 10: Frequency response of wave-induced forces and moments of dual submerged horizontal porous flexible plates for $x_1/h = -0.75$, $x_2/h = 0.75$, $a_1/h = a_2/h = 0.5$, $d_1/h + d_2/h = 0.3$ and different relative vertical positions of the two plates in terms of d_1/d_2 ranging between 1/2 to 2/1: (a) $\bar{F}_1$; (b) $\bar{F}_2$; (c) $\bar{M}_1$; and (d) $\bar{M}_2$.

amplifying moment. Corroborating this, $|M_1|$ peaks in this band (Fig. 12c). Analogous force/moment behaviour occurs for Plate 2 when configured as the longest plate with $a_1/a_2 = 1/3$.

4.2. Metastructure consisting of rigid horizontal plate arrays

This subsection analyses four metastructure configurations, and is based on previous analysis of metastructures composed of parallel rigid plates (see e.g. [32, 21]). As shown in Fig. 13, the metastructure configurations have circular, square, trapezoidal, and inverted trapezoidal cross-sections. Crucially, all possess identical cross-sectional areas ($0.25h^2$) and aligned centroids ($z = -0.5h$). Each metastructure comprises nine rigid horizontal plates separated by a vertical gap of $h/16$. We consider two permeability conditions: fully impermeable plates ($p_n = 0$); and porous plates characterised by $2\pi p_n/k = 5.0$.

Figures 14 and 15 show the frequency responses of $|R|$, $|T|$, η_{diss}, total wave-induced force ($F_0 = \sum_1^9 F_n$), and total wave-induced moment ($M_0 = \sum_1^9 M_n$) for the four metastructures. For impermeable plates, no wave power is dissipated ($\eta_{diss} = 0$), and peaks in the $|R| - kh$ curve align with troughs in $|T| - kh$. Among

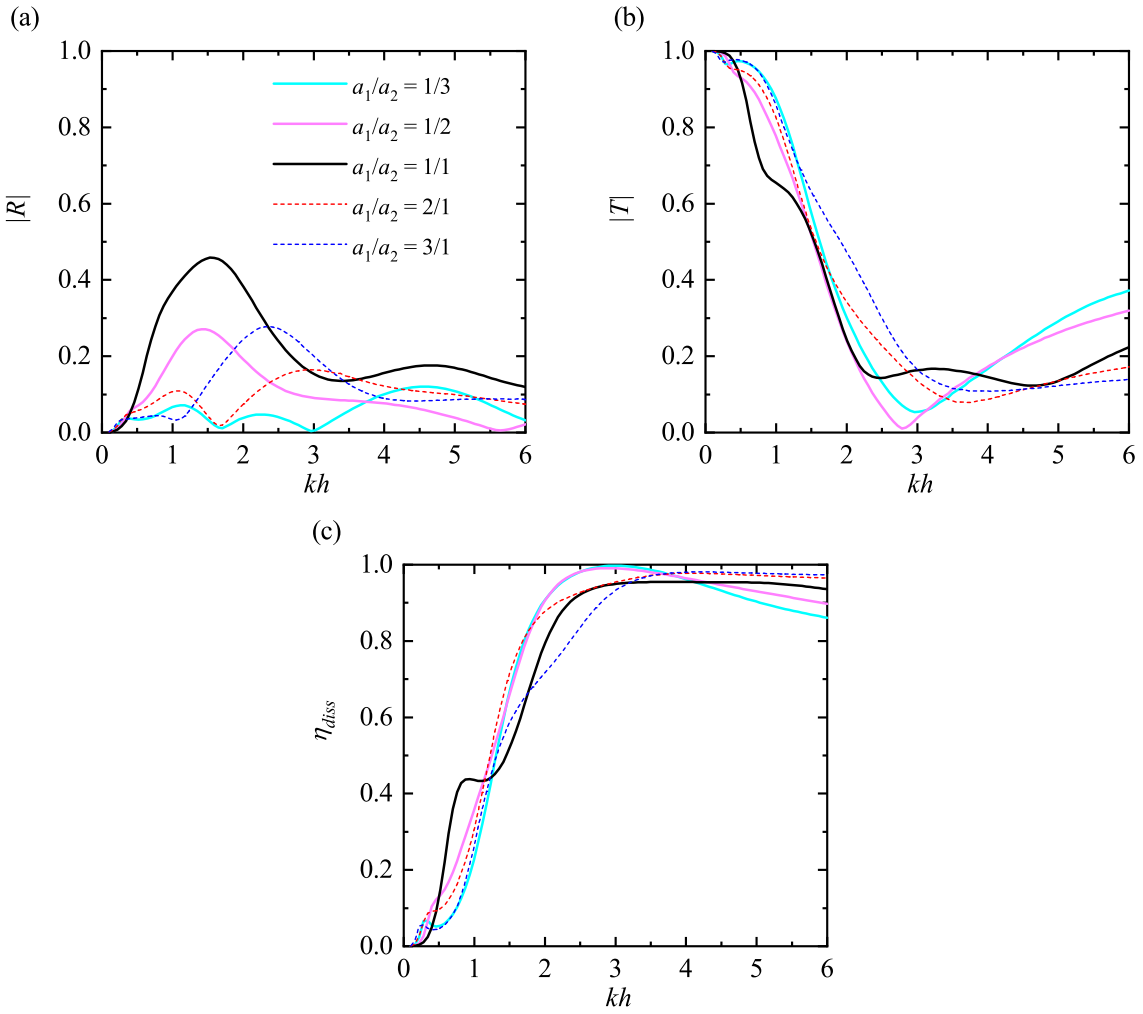

Figure 11: Frequency response of reflection coefficients, transmission coefficients, and wave power dissipation coefficients of dual submerged horizontal porous flexible plates for $x_1 = x_2 = 0$, $a_1/h + a_2/h = 1.0$ $d_1/h = 0.1$, $d_2/h = 0.2$, and different length ratios of the two plates in terms of a_1/a_2 ranging between 1/3 to 3/1: (a) $|R|$; (b) $|T|$; and (c) η_{diss}.

the configurations, the inverted trapezoid exhibits the strongest reflection peak ($|R| = 0.44$) at the lowest frequency ($kh = 2.0$). The frequency responses of F_0 are similar (see Fig. 15a) because this configuration contains the longest plate within the metastructure at shallowest submergence depth. However, for short waves ($kh > 4.0$), the value of $|R|$ is smallest. For short-wavelength waves, fluid motion is confined near the free surface. The top plate of the inverted trapezoid is submerged deeper than in other designs, and so it interacts less with these high-frequency waves, leading to a lower reflection coefficient. Conversely, long-wavelength waves engage the entire metastructure. In this regime, shallower and longer plates produce stronger interactions, which is why the inverted trapezoid configuration is most effective at reflecting low-frequency waves. In particular, incident waves are perfectly transmitted ($|R| = 0$) at $kh = 5.0$. For $2.8 < kh < 6.0$, the square cross-section metastructure reflects more wave power than the other three configurations. Both the total wave-induced force $|F_0|$ and, more significantly, the total wave-induced moment $|M_0|$ acting on the inverted trapezoidal metastructure exceed those of other configurations. This

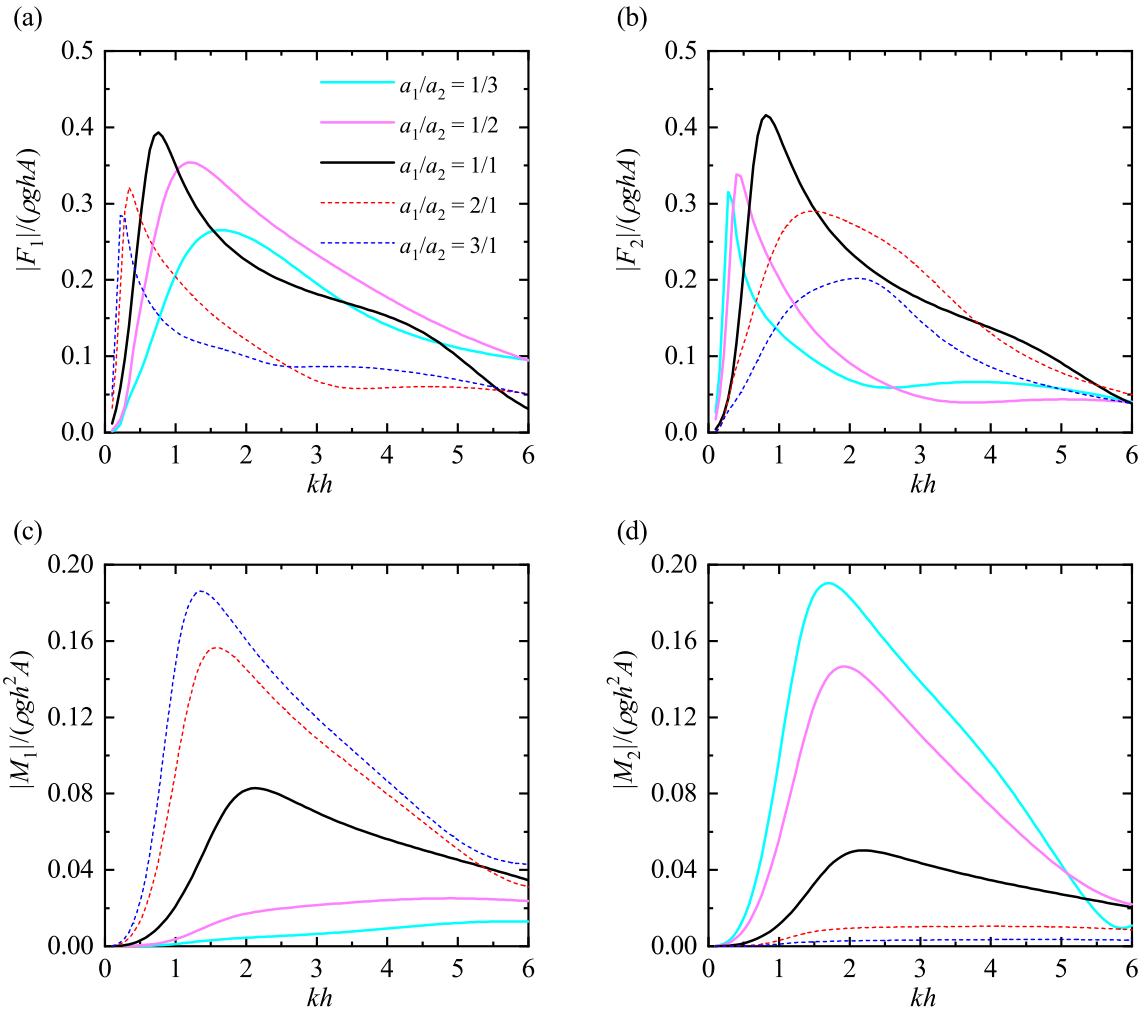

Figure 12: Frequency response of the wave-induced forces and moments of dual submerged horizontal porous flexible plates for $x_1 = x_2 = 0$, $a_1/h + a_2/h = 1.0$ $d_1/h = 0.1$, $d_2/h = 0.2$, and different length ratios of the two plates in terms of a_1/a_2 ranging between 1/3 to 3/1: (a) $\bar{F}_1$; (b) $\bar{F}_2$; (c) $\bar{M}_1$; and (d) $\bar{M}_2$.

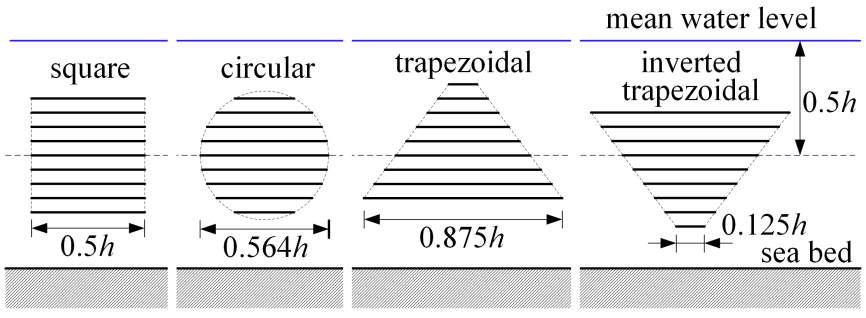

Figure 13: Sketch showing the circular, square, trapezoidal, and inverted trapezoidal cross-sections of the four metastructures of interest. The area of each cross-section is $0.25h^2$; the channel width (i.e., distance between adjacent plates) is $h/16$, the number of plates is $N = 9$, and the centroid of the structure is located at $z = -0.5h$.

increased loading could constrain the applicability of the inverted trapezoidal metastructure in engineering practice.

When the plates are porous ($2\pi p_n/k = 5.0$), wave power dissipation occurs. Consequently, $|R|$, $|T|$, $|F_0|$, and $|M_0|$ all decrease significantly across nearly all examined kh values for all the metastructures considered herein. An exception is the inverted trapezoid, where $|R|$ exhibits a modest increase when $kh \approx 5.0$. Across the bandwidth $2.0 < kh < 5.5$, the inverted trapezoidal metastructure achieves the highest dissipation efficiency (η_{diss}), followed by the square and circular metastructures. The trapezoidal configuration dissipates least power. The porous inverted trapezoid provides the best coastal defence in terms of wave transmission, which is minimal over most of the studied frequency range. Designers must note the associated increase in cost owing to the larger wave forces and moments. The wave attenuation performance may be improved by reducing the plate submergence depth. Furthermore, it should be noted that the porosity value $2\pi p_n/k = 5.0$ was selected arbitrarily in this study. An optimal porosity likely exists to maximise wave power dissipation, which would enhance the overall wave attenuation capability of these metastructures.

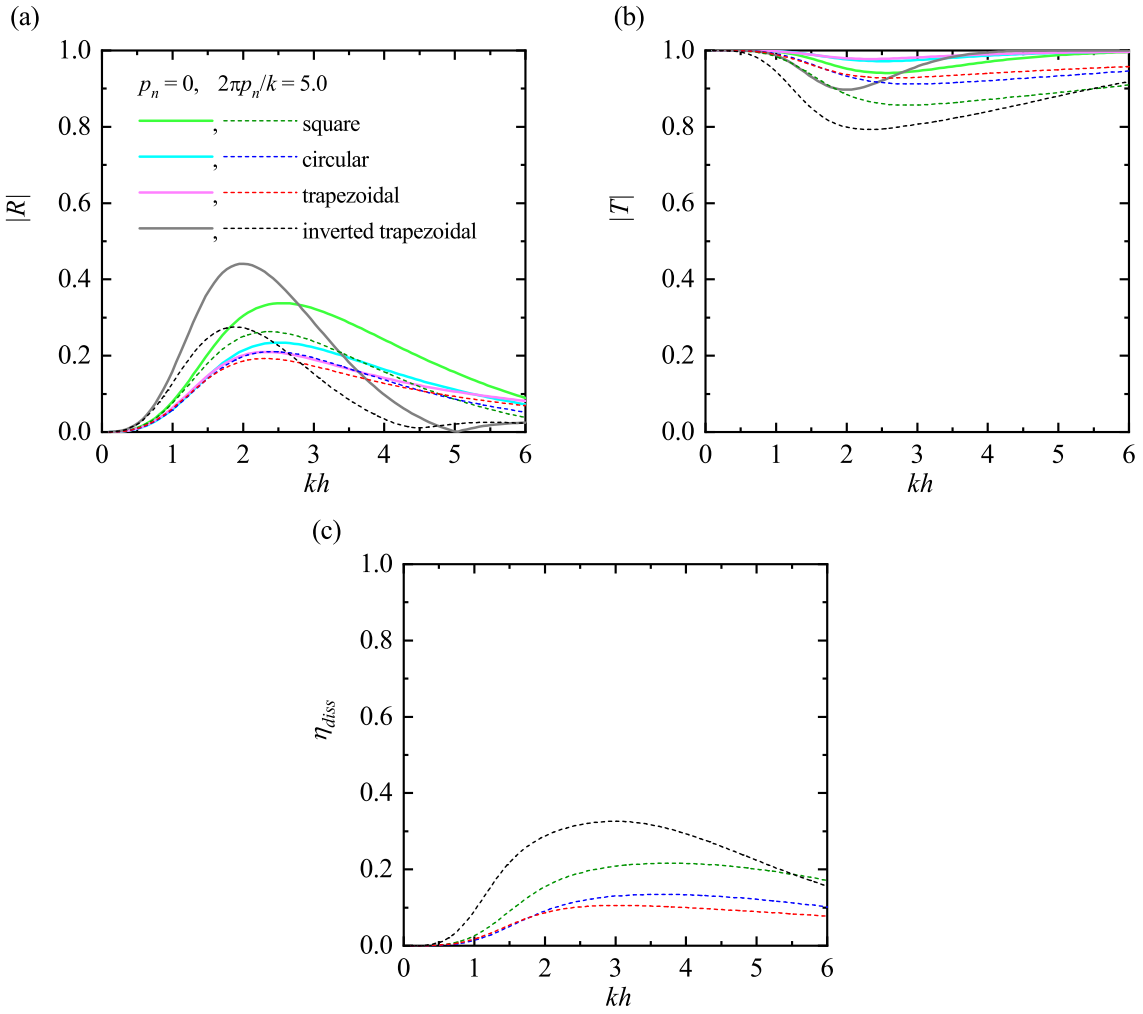

Figure 14: Frequency response of reflection coefficients, transmission coefficients, and wave power dissipation coefficients of four different meta structures consisting of horizontal rigid/porous plates: (a) $|R|$; (b) $|T|$; and (c) η_{diss}.

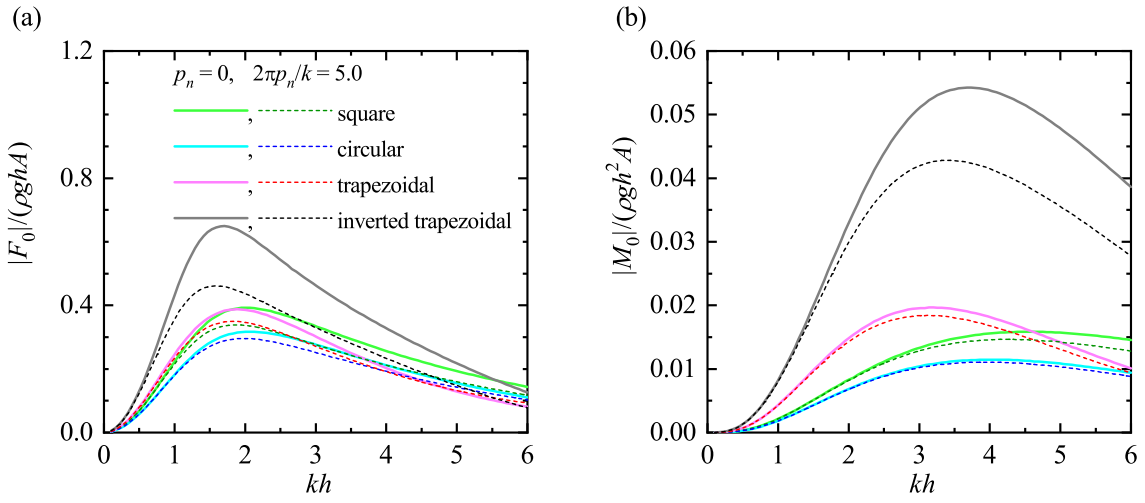

Figure 15: Frequency response of wave-induced forces and moments of four different meta structures consisting of horizontal rigid/porous plates: (a) wave excitation force; and (b) wave excitation moment.

5. Conclusions

This paper has presented a study of water wave scattering by arrays of submerged horizontal plates and membranes. The plates have either rigid or elastic forms. Both the plates and membranes can be impermeable or porous, with the membranes under tension. The core contribution of the paper is a theoretical model derived from linear potential flow theory using the Fourier transform. Our model overcomes a limitation of previous eigenfunction matching methods by enabling the analysis of arbitrarily arranged plates (coaxial, staggered, side-by-side). The velocity potential discontinuity across each plate or membrane is represented by an expansion in Chebyshev polynomials of the second kind. This efficiently resolves the inherent square-root edge behaviour, leading to rapid solution convergence.

The model is verified for three sets of benchmark tests: (i) boundary element method predictions of flexible membrane wave scattering [12], (ii) semi-analytical solutions obtained using the eigenfunction matching method for flexible plate scattering [13, 19], and (iii) boundary element method solutions for dual coaxial rigid plates [24]. Excellent agreement is achieved in all cases. Additionally, predictions of wave power dissipation for staggered dual porous flexible plates, obtained via direct and indirect methods, show consistent convergence.

A parameter study was undertaken using the verified model to predict wave interactions with pairs of submerged porous flexible plates, and wave interactions with metastructures composed of horizontal rigid plate arrays with square, circular, trapezoidal, and inverted trapezoidal cross-sectional configurations. Our model proved theoretically that exchanging the horizontal positions of two staggered porous flexible plates or membranes does not alter the wave transmission coefficient at any wave frequency. It was found that coaxial arrangements of dual porous flexible plates exhibit bimodal peaks in the frequency response of the reflection coefficient, whereas staggered or side-by-side configurations shift the peaks toward lower frequencies and enhance the attenuation of short waves. Wave-induced force and moment oscillations on seaward plates intensify with plate separation due to wave interference. It was also found that the vertical

position ratio (d_1/d_2) non-monotonically affects the reflection of side-by-side dual porous flexible plates, with shallower seaward plates amplifying reflection at $kh \approx 0.75$ and 5.40 but reducing it at $kh \approx 3.75$. Additional wave power is dissipated for $1.5 < kh < 4.5$ when the seaward plate is shallower. The length ratio (a_1/a_2) critically tunes the performance of dual coaxial plates, with a ratio of 1/3 achieving near-total dissipation ($|R|, |T| \approx 0$) at $kh = 3.0$. Longer plates with shallow submergence improve attenuation of short incident waves by intercepting surface-propagated wave energy.

Our model shows that cross-section geometrical configuration governs the frequency-selective behaviour of metastructures consisting of multiple rigid horizontal plates. Inverted trapezoids maximise low-frequency reflection due to extended shallow-depth plates but minimise short-wave interaction with deeper top plates. Square cross-sections are most reflective for $2.8 < kh < 6.0$. For a porosity of $2\pi p_n/k = 5.0$, the values of $|R|$, $|T|$, and structural loads are notably reduced and dissipation enhanced. The inverted trapezoid achieves peak dissipation (η_{diss}) for $2.0 < kh < 5.5$, surpassing square, circular, and trapezoidal configurations. The inverted trapezoid configuration incurs the highest force and moment loads (especially the latter), potentially limiting practical deployment despite its wave-dissipation superiority.

The proposed model could be extended to assess the performance of typical marine structures comprising horizontal plates and/or membranes. The present model is limited to solving 2D problems, assuming the plates/membranes to be infinitely long in the y direction. Finite width alters the plate/membrane hydroelastic behavior, and future work is therefore recommended to extend the present 2D model to 3D. The present work assumes that the initial membrane tension is sufficiently large that dynamic tension effects may be neglected. However, practical tension ranges depend on the plate/membrane material and the exact application, thus affecting stability prediction. Importantly, these practical aspects must be considered by designers. In future work, we intend to consider wave interaction with a submerged flexible plate or membrane in a channel, wave-current interactions with submerged plates and/or membranes, and wave scattering by hybrid arrays of horizontal plates and membranes (including both surface-piercing and submerged components).

Acknowledgement: The work was supported by the UK EPSRC Grant EP/V040367/1-"Flexible Responsive Systems in Wave Energy: FlexWave". DMG also gratefully acknowledges the EPSRC for supporting part of this work through the Supergen ORE Hub, United Kingdom, EP/S000747/1.

Appendix A. Some useful properties of the second-kind Chebyshev polynomial $U_p(u)$

Some useful results regarding the Chebyshev polynomials of the second kind, U_p, that can be inferred include (see e.g. [29, §7.34, 7.35])

$$\frac{\mathrm{d}^2}{\mathrm{d}u^2}\int_{-1}^{1}\ln|u-u'|\sqrt{1-u'^2}U_p(u')\mathrm{d}u' = \pi(p+1)U_p(u), \quad |u|\le 1 \tag{A.1}$$

and

$$\int_{-1}^{1}\mathrm{e}^{\mathrm{i}\lambda u}\sqrt{1-u^2}U_p(u)\mathrm{d}u = \frac{\mathrm{i}^p(p+1)\pi}{\lambda}\mathrm{J}_{p+1}(\lambda). \tag{A.2}$$

with which we have

$$\begin{aligned}&\frac{\mathrm{d}^2}{\mathrm{d}u^2}\int_{x_n-a_n}^{x_n+a_n}\ln|u-u'|\sqrt{1-\left(\frac{u'-x_n}{a_n}\right)^2}U_p\left(\frac{u'-x_n}{a_n}\right)\mathrm{d}u'\\&=\frac{\pi(p+1)U_p[(u-x_n)/a_n]}{a_n},\quad |u-x_n|\le a_n,\end{aligned}\tag{A.3}$$

$$\int_{x_n-a_n}^{x_n+a_n}U_p\left(\frac{x-x_n}{a_n}\right)w_{p'}^*\left(\frac{x-x_n}{a_n}\right)\mathrm{d}x=\frac{\delta_{p,p'}(-\mathrm{i})^{p'}a_n}{2(p'+1)},\tag{A.4}$$

$$\int_{x_n-a_n}^{x_n+a_n}w_p\left(\frac{x-x_n}{a_n}\right)\mathrm{e}^{-\mathrm{i}lx}\mathrm{d}x=\frac{\mathrm{e}^{-\mathrm{i}x_nl}\mathrm{J}_{p+1}(la_n)}{l},\tag{A.5}$$

and

$$\int_{x_n-a_n}^{x_n+a_n}w_p\left(\frac{x-x_n}{a_n}\right)w_{p'}^*\left(\frac{x-x_n}{a_n}\right)\mathrm{d}x=\frac{\mathrm{i}^{p-p'}a_nU_{p,p'}}{(p+1)(p'+1)\pi^2},\tag{A.6}$$

where

$$\begin{aligned}U_{p,q}&=\int_{-1}^{1}(1-u^2)U_p(u)U_q(u)\mathrm{d}u\\&=\begin{cases}0, & (p-q)\text{ is odd}\\ \dfrac{1}{2}\left(\dfrac{1}{p-q+1}-\dfrac{1}{p-q-1}-\dfrac{1}{p+q+3}+\dfrac{1}{p+q+1}\right), & (p-q)\text{ is even}\end{cases}\end{aligned}\tag{A.7}$$

Appendix B. Invariance property of transmission coefficients

For an array of horizontal rigid plates, Eq. (39) can be rewritten as

$$\begin{aligned}&\mathrm{i}p_ja_j\sum_{p=0}^{\infty}b_{j,p}\frac{\mathrm{i}^{p+p'}(-1)^{p'}U_{p,p'}}{(p+1)(p'+1)\pi^2}-\frac{1}{4\pi(p'+1)}b_{j,p'}-\frac{1}{2\pi}\sum_{n=1}^{N}\sum_{p=0}^{\infty}b_{n,p}\mathrm{e}^{\mathrm{i}k(x_n-x_j)}K_{n,j,p,p'}\\&+\frac{\mathrm{i}}{2k}\sinh[k(h-d_j)]\mathrm{J}_{p'+1}(ka_j)\sum_{n=1}^{N}\sum_{p=0}^{\infty}b_{n,p}\mathrm{J}_{p+1}(ka_n)[1+(-1)^{p+p'}\mathrm{e}^{2\mathrm{i}k(x_n-x_j)}]s_n(k)\\=&\frac{\mathrm{i}gA\sinh[k(h-d_j)]\mathrm{J}_{p'+1}(ka_j)}{\omega\cosh(kh)}\end{aligned}\tag{B.1}$$

where $b_{n,p}=\mathrm{e}^{-\mathrm{i}kx_n}a_{n,p}$ and is solved using

$$\vec{X}=\frac{\mathrm{i}gA}{\omega\cosh(kh)}\mathbf{S}^{-1}\vec{Y},\tag{B.2}$$

in which $\mathbf{S}$ is the coefficient matrix of Eq. (B.1), and

$$\vec{X}=\{b_{n,p}\},\quad \vec{Y}=\{\sinh[k(h-d_n)]\mathrm{J}_{p+1}(ka_n)\}.\tag{B.3}$$

After inserting Eq. (37) into Eq. (25), and employing Eqs. (B.2) and (B.3), we have

$$T=1-\frac{\mathrm{i}}{2khN_0}\vec{Y}^T\mathbf{S}^{-1}\vec{Y}=1-\frac{\mathrm{i}}{2khN_0}\vec{Y}^T\mathbf{S}^{T^{-1}}\vec{Y}.\tag{B.4}$$

The symmetry relations $(-1)^{p'}U_{p,p'}=(-1)^pU_{p',p}$, $K_{n,j,p,p'}(x_j,x_n)=K_{j,n,p',p}(-x_n,-x_j)$ imply that the coefficient matrix $\mathbf{S}$ obeys element-wise symmetry $S_{j,p';n,p}(x_j,x_n)=S_{n,p;j,p'}(-x_n,-x_j)$, leading to the global matrix property $\mathbf{S}(x_j,x_n)=\mathbf{S}(-x_j,-x_n)^T$. When substituted into Eq. (B.4), this symmetry ensures that the transmission coefficient T remains invariant under a mirror-symmetric reconfiguration of the plate array across the $x=0$ plane.

This invariance property also holds for systems involving flexible plates and/or membranes.

References

[1] A.-C. Tsiaras, T. Karambas, D. Koutsouvela, Design of detached emerged and submerged breakwaters for coastal protection: Development and application of an advanced numerical model, J. Waterw. Port Coast. Ocean Eng. 146 (4) (2020) 04020012.

[2] R. Ranasinghe, I. L. Turner, Shoreline response to submerged structures: A review, Coastal Engineering 53 (1) (2006) 65–79.

[3] Y. Stender, M. Foley, K. Rodgers, P. Jokiel, A. Singh, Evaluating the feasibility and advantage of a multi-purpose submerged breakwater for harbor protection and benthic habitat enhancement at Kahului Commercial Harbor, Hawai'i: case study, SN Appl. Sci. 3 (2) (2021) 167.

[4] M. McIver, Diffraction of water waves by a moored, horizontal, flat plate, J. Engng Math. 19 (1985) 297–319.

[5] N. Parsons, P. Martin, Scattering of water waves by submerged plates using hypersingular integral equations, Appl. Ocean Res. 14 (5) (1992) 313–321.

[6] R. Porter, Linearised water wave problems involving submerged horizontal plates, Appl. Ocean Res. 50 (2015) 91–109.

[7] X. Yu, A. T. Chwang, Water waves above submerged porous plate, J. Engng Mech. 120 (6) (1994) 1270–1280.

[8] Y. Liu, Y. Li, An alternative analytical solution for water-wave motion over a submerged horizontal porous plate, J. Engng Math. 69 (2011) 385–400.

[9] D. V. Evans, M. A. Peter, Asymptotic reflection of linear water waves by submerged horizontal porous plates, J. Engng Math. 69 (2011) 135–154.

[10] S. An, O. M. Faltinsen, Linear free-surface effects on a horizontally submerged and perforated 2D thin plate in finite and infinite water depths, Appl. Ocean Res. 37 (2012) 220–234.

[11] I. Cho, M. Kim, Transmission of oblique incident waves by a submerged horizontal porous plate, Ocean Engng 61 (2013) 56–65.

[12] I. H. Cho, M. H. Kim, Interactions of a horizontal flexible membrane with oblique waves, J. Fluid Mech. 367 (1998) 139–161.

[13] M. Ul-Hassan, M. Meylan, M. Peter, Water-wave scattering by submerged elastic plates, Q. J. Mech. Appl. Maths 62 (3) (2009) 321–344.

[14] T. D. Williams, M. H. Meylan, The Wiener–Hopf and residue calculus solutions for a submerged semi–infinite elastic plate, J. Engng Math. 75 (2012) 81–106.

[15] I. H. Cho, M. H. Kim, Interactions of horizontal porous flexible membrane with waves, J. Waterw. Port Coast. Ocean Eng. 126 (5) (2000) 245–253.

[16] H. Behera, T. Sahoo, Hydroelastic analysis of gravity wave interaction with submerged horizontal flexible porous plate, J. Fluids Struct. 54 (2015) 643–660.

[17] E. Renzi, Hydroelectromechanical modelling of a piezoelectric wave energy converter, Proc. R. Soc. A 472 (2016) 20160715.

[18] F. Buriani, E. Renzi, Hydrodynamics of a flexible piezoelectric wave energy harvester moored on a breakwater, in: 12th European Wave and Tidal Energy Conference (EWTEC), Cork, Ireland, 2017.

[19] S. Zheng, M. Meylan, X. Zhang, G. Iglesias, D. Greaves, Performance of a plate-wave energy converter integrated in a floating breakwater, IET Renew. Power Gener. 15 (14) (2021) 3206–3219.

[20] S. Zheng, H. Liang, S. Michele, D. Greaves, Water wave interaction with an array of submerged circular plates: Hankel transform approach, Phys. Rev. Fluids 8 (2023) 014803.

[21] H. Liang, R. Porter, S. Zheng, Wave scattering by plate array metacylinders of arbitrary cross-section, J. Fluid Mech. 1001 (2024) A6.

[22] K.-H. Wang, Q. Shen, Wave motion over a group of submerged horizontal plates, Intl J. Engng Science 37 (6) (1999) 703–715.

[23] Y. Liu, Y. Li, B. Teng, S. Dong, Wave motion over a submerged breakwater with an upper horizontal porous plate and a lower horizontal solid plate, Ocean Engng 35 (16) (2008) 1588–1596.

[24] I. Cho, H. Koh, J. Kim, M. Kim, Wave scattering by dual submerged horizontal porous plates, Ocean Engng 73 (2013) 149–158.

[25] Z. Fang, L. Xiao, T. Peng, Generalized analytical solution to wave interaction with submerged multi-layer horizontal porous plate breakwaters, J. Engng Math. 105 (1) (2017) 117–135.

[26] T. Mirza, M. Ul-Hassan, The study of water wave scattering by series of submerged elastic scatterers, Phys. Fluids 36 (8) (2024) 087111.

[27] B. Wilks, M. H. Meylan, A numerical comparison of eigenfunction matching and singularity-respecting Galerkin approximation methods for linear water wave scattering, J. Mar. Sci. Eng. 13 (3) (2025).

[28] M. H. Meylan, L. G. Bennetts, M. A. Peter, Water-wave scattering and energy dissipation by a floating porous elastic plate in three dimensions, Wave Motion 70 (2017) 240–250.

[29] I. S. Gradshteyn, I. M. Ryzhik, Table of integrals, series, and products, 7th Edition, Academic Press, 2007.

[30] S. Zheng, M. H. Meylan, D. Greaves, G. Iglesias, Water-wave interaction with submerged porous elastic disks, Phys. Fluids 32 (4) (2020) 047106.

[31] S. Zheng, Y. Zhang, Analytical study on hydrodynamic performance of a raft-type wave power device, J. Mar. Sci. Technol. 22 (2017) 620–632.

[32] S. Zheng, H. Liang, D. Greaves, Wave scattering and radiation by a surface-piercing vertical truncated metamaterial cylinder, J. Fluid Mech. 983 (2024) A7.